Pyritic stromatolites from the Paleoarchean Dresser Formation, Pilbara Craton: Resolving biogenicity and hydrothermally influenced ecosystem dynamics

Raphael Baumgartner, Martin van Kranendonk, Stefano Caruso, Kathleen Campbell, Michaela Dobson, Bronwyn Teece, Michael Verrall, Martin Homann, Stefan Lalonde, Pieter Visscher

Received: 12 July 2023 | Revised: 13 June 2024 | Accepted: 24 June 2024

DOI: 10.1111/gbi.12610

ORIGINAL ARTICLE

gebiology WILEY

Pyritic stromatolites from the Paleoarchean Dresser Formation, Pilbara Craton: Resolving biogenicity and hydrothermally influenced ecosystem dynamics

Raphael J. Baumgartner[1,2] | Martin J. Van Kranendonk[2,3] | Stefano Caruso[1,2] | Kathleen A. Campbell[4] | Michaela J. Dobson[4] | Bronwyn L. Teece[2,5] | Michael Verrall[1] | Martin Homann[6] | Stefan Lalonde[7] | Pieter T. Visscher[8]

[1]CSIRO Mineral Resources, Australian Resources Research Centre, Kensington, Western Australia, Australia

[2]School of Biological, Earth and Environmental Sciences, Australian Centre for Astrobiology, The University of New South Wales, Kensington, New South Wales, Australia

[3]School of Earth and Planetary Sciences, Curtin University, Bentley, Western Australia, Australia

[4]School of Environment and Te Ao Mārama, Centre for Fundamental Inquiry, University of Auckland, Auckland, New Zealand

[5]Origins and Habitability Laboratory, NASA Jet Propulsion Laboratory, California Institute of Technology, Pasadena, California, USA

[6]Department of Earth Sciences, University College London, London, UK

[7]European Institute for Marine Studies, Technopôle Brest-Iroise, Plouzané, France

[8]Department of Marine Sciences, University of Connecticut, Groton, Connecticut, USA

Correspondence
Raphael J. Baumgartner, CSIRO Mineral Resources, Australian Resources Research Centre, Kensington, Western Australia, Australia.
Email: raphael.baumgartner@csiro.au

Abstract

This study investigates the paleobiological significance of pyritic stromatolites from the 3.48 billion-year-old Dresser Formation, Pilbara Craton. By combining paleoenvironmental analyses with observations from well-preserved stromatolites in newly obtained drill cores, the research reveals stratiform and columnar to domal pyritic structures with wavy to wrinkly laminations and crest thickening, hosted within facies variably influenced by syn-depositional hydrothermal activity. The columnar and domal stromatolites occur in strata with clearly distinguishable primary depositional textures. Mineralogical variability and fine-scale interference textures between the microbialites and the enclosing sediment highlight interplays between microbial and depositional processes. The stromatolites consist of organomineralization – nanoporous pyrite and microspherulitic barite – hosting significant thermally mature organic matter (OM). This includes filamentous organic microstructures encased within nanoporous pyrite, resembling the extracellular polymeric substance (EPS) of microbes. These findings imply biogenicity and support the activity of microbial life in a volcano-sedimentary environment with hydrothermal activity and evaporative cycles. Coupled changes in stromatolite morphology and host facies suggest growth in diverse niches, from dynamic, hydrothermally influenced shallow-water environments to restricted brine pools strongly enriched in SO_4^{2-} from seawater and hydrothermal activity. These observations, along with S stable isotope data indicating influence by S metabolisms, and accumulations of biologically significant metals and metalloids (Ni and As) within the microbialites, help constrain microbial processes. Columnar to domal stromatolites in dynamic, hydrothermally influenced shallow water deposits likely formed by microbial communities dominated by phototrophs. Stratiform pyritic structures within barite-rich strata may reflect the prevalence of chemotrophs near hydrothermal venting, where hydrothermal activity and microbial processes influenced barite precipitation. Rapid pyrite precipitation, a putative taphonomic process for preserving

microbial remnants, is attributed to microbial sulfate reduction and reduced S sourced from hydrothermal activity. In conclusion, this research underscores the biogenicity of the Dresser stromatolites and advances our understanding of microbial ecosystems in Earth's early history.

KEYWORDS
biogenicity, Dresser Formation, ecosystem dynamics, microbe–environment interactions, Paleoarchean, stromatolites

1 | INTRODUCTION

The East Pilbara Terrane (Pilbara Craton, Western Australia) offers compelling evidence for the early emergence of life on Earth. This evidence includes: (i) ancient microstructures resembling fossilized microorganisms, yet their interpretation can be controversial (e.g., Brasier et al., 2002; Schopf & Packer, 1987) and (ii) less contentious, but not universally accepted, macroscopic stromatolites. This study, which focuses on stromatolites from the c. 3.48 billion-year-old (Ga) Dresser Formation in the North Pole Dome of the East Pilbara Terrane (Baumgartner et al., 2019; Buick et al., 1981; Hickman-Lewis et al., 2023; Van Kranendonk, 2011; Van Kranendonk et al., 2008; Walter et al., 1980), classifies stromatolites as morphologically distinct, "laminated organo-sedimentary structures formed by trapping/binding of sediment and/or mineral precipitation induced by microbial communities (Walter, 1976)".

The ancient stromatolites of the East Pilbara Terrane exhibit diverse morphologies, including stratiform, columnar, domal, or conical, typically with smooth, wavy, or wrinkly internal laminations (e.g., Allwood et al., 2006, 2009; Baumgartner et al., 2019; Buick et al., 1981; Flannery et al., 2018; Grey & Awramik, 2020; Hofmann et al., 1999; Lowe, 1980; Van Kranendonk, 2011; Van Kranendonk et al., 2003, 2008, 2019; Walter, 1976). A key for identifying Archean macroscopic stromatolites is distinguishing them from, and demonstrating their interference with, contemporaneous depositional textures (e.g., Van Kranendonk, 2011; Van Kranendonk et al., 2019). Microanalytical characterizations aid in assessing biogenicity, documenting micromorphological and microtextural characteristics, chemical compositions, isotopic signatures, physical traces of microbes (including putative microbial remnants and decomposed organic material), and distinctive mineralogical characteristics, including mineral-organic assemblages representing biomineralization or precipitation onto microbial substrates (e.g., Baumgartner et al., 2019; Baumgartner, Van Kranendonk, Fiorentini, et al., 2020; Duda et al., 2016; Flannery et al., 2018; Lepot et al., 2008; Marin-Carbonne et al., 2018; Sforna et al., 2014).

While the stromatolites of the East Pilbara Terrane provide significant evidence of ancient life, debates persist due to skepticism about the reliability of morphology and texture as criteria for biogenicity (e.g., Bosak et al., 2021; Neveu et al., 2018). Such concerns also exist for the c. 3.48 Ga Dresser stromatolites (see Lowe, 1994, and the reply by Bosak et al., 2021; Buick et al., 1995), despite their occurrence in facies indicative of habitable environments, and their morphological and textural characteristics – stratiform, columnar, domal, and occasionally conical, featuring smooth, wavy, or wrinkly laminated architectures – that align with bona fide stromatolites throughout the geological record. Challenges in constraining biogenicity include the weathering of surface outcrops, which has transformed the stromatolites into secondary mineral associations rich in iron oxide-hydroxides (Buick & Dunlop, 1990; Van Kranendonk et al., 2008). Hydrothermal alteration, metamorphism, and weathering have also altered chemical and isotopic signatures, including the C stable isotope signature and molecular structure of OM (Baumgartner et al., 2019; Van Kranendonk et al., 2008).

Pyritic Dresser stromatolites from well-preserved drill cores exhibit characteristics not preserved on the surface (Baumgartner et al., 2019; Van Kranendonk et al., 2008). These columnar to stratiform stromatolites contain significant OM, including putative EPS remnants within pyrite and barite organomineralization (Baumgartner et al., 2019; Baumgartner, Van Kranendonk, Fiorentini, et al., 2020). Organic C and S stable isotope signatures align with isotopic fractionation by biological processes (Baumgartner et al., 2019; Baumgartner, Caruso, Fiorentini, et al., 2020). Accumulations of specific transition metals and metalloids within the stromatolites, particularly Ni, As, and Zn derived from sedimentary and hydrothermal sources (Baumgartner, Caruso, Fiorentini, et al., 2020), are consistent with growth in a volcano-sedimentary setting influenced by hydrothermal activity (Caruso et al., 2021, 2023; Djokic et al., 2017, 2021, 2024; Nijman et al., 1998; Tadbiri & Van Kranendonk, 2020; Van Kranendonk, 2006, 2011; Van Kranendonk et al., 2008, 2019; Van Kranendonk & Pirajno, 2004). Observations on bedded cherts and hydrothermal veins provide additional evidence for ancient life. Potential microfossils and the C stable isotope signatures of OM and CO_2-CH_4-bearing fluid inclusions are consistent with microbial activity (Duda et al., 2018; Glikson et al., 2008; Ueno et al., 2004, 2006; Ueno, Isozaki, et al., 2001; Ueno, Maruyama, et al., 2001). The S stable isotope signatures of barite-pyrite precipitates demonstrate influences by S metabolizing processes (e.g., Philippot et al., 2007; Shen et al., 2001, 2009; Ueno et al., 2008).

The overview above highlights the progress in understanding the origins of the Dresser stromatolites. However, questions remain due to the limited availability of well-preserved specimens in drill cores, which have yet to capture the diverse morphologies and depositional contexts observed in surface outcrops (e.g., compare the findings in

Baumgartner et al., 2019; Van Kranendonk et al., 2008, with those in Buick et al., 1981; Van Kranendonk, 2006, 2011; Walter et al., 1980). Additionally, prior drill core analyses have not comprehensively investigated the dynamics of microbial ecosystems. Addressing these gaps, this study leverages prior research on the pyritic Dresser stromatolites and integrates knowledge of their depositional context with new observations from relatively unweathered specimens in drill cores. Supported by microanalytical characterizations, we describe distinct pyritic structures displaying morphological and textural variations indicative of accretion under different conditions. The stromatolites mainly consist of organic-mineral associations, including organic microstructures resembling microbial remnants. This high-quality preservation establishes the Dresser microbialites as a cornerstone for understanding life during the Paleoarchean era.

2 | GEOLOGICAL SETTING

The Dresser Formation occurs as a circular, shallow-dipping unit in a ring of hills that form the North Pole Dome in the East Pilbara Terrane of the Pilbara Craton (Figure S1). Dated at 3481 ± 4 Ma (Van Kranendonk et al., 2008), this formation is part of the Warrawoona Group, which dates to c. 3520–3430 Ma and is the lowest of four groups in the Pilbara Supergroup (Van Kranendonk et al., 2007). The Dresser Formation lies conformably on the c. 3490 Ma North Star Basalt and is overlain by the c. 3470 Ma Mount Ada Basalt. The 3454 ± 17 Ma North Pole Monzogranite (Asanuma et al., 2018) is emplaced into the North Star Basalt at the core of the North Pole Dome (Figure S1). The Dresser Formation consists of three units. At its base lies the bedded chert-barite unit, also known as the "North Pole Chert member". This unit, spanning 1–250 m in thickness, includes diverse stromatolites, interbedded black, grey, and white cherts, layers of coarsely crystalline barite, siliceous hot spring deposits, lacustrine and fluvial deposits, jaspilitic cherts, bedded carbonate-chert, epiclastic volcanics, conglomerates, and sandstones that display ripple marks and desiccation cracks (Buick & Dunlop, 1990; Djokic et al., 2017, 2021; Van Kranendonk et al., 2008, 2019). The overlying unit comprises pillow basalt and dolerite, 1–2 km thick, with an interbedded unit of bedded jaspilitic chert and local chert pebble conglomerate. The "Upper Chert member", which comprises bedded cherts with epiclastic sedimentary rocks, was deposited under deep water conditions (Nijman et al., 1998; Van Kranendonk et al., 2008, 2019).

The North Star Basalt underlying the Dresser Formation hosts extensive hydrothermal silica-barite veins (Figure S1), with the largest veins occurring within listric normal growth faults (Caruso et al., 2021; Nijman et al., 1998; Tadbiri & Van Kranendonk, 2020). These veins, reaching widths of up to c. 20 m, extend deep into the basaltic footwall. Four distinct sets of early veins have been identified, three of which terminate within the lower part of the North Pole Chert member. The youngest veins, bound to the largest listric growth faults, cut through to the top of the formation. These characteristics demonstrate that most veins were emplaced contemporaneously with the deposition of the Dresser Formation (Nijman et al., 1998; Tadbiri & Van Kranendonk, 2020; Van Kranendonk & Pirajno, 2004). Specifically, the geometries of the vein networks imply emplacement within a volcanic caldera setting, characterized by multiple collapse centers (i.e., piecemeal caldera; Tadbiri & Van Kranendonk, 2020; Van Kranendonk et al., 2008). Analyses of crack-seal textured veins, indicative of multiple fluid pulses, yielded temperature estimates of c. 150–350°C, lowest at the tops of the veins (Harris et al., 2009; Ueno, Isozaki, et al., 2001; Ueno, Maruyama, et al., 2001; Van Kranendonk & Pirajno, 2004). The barite is restricted to the upper sections of the veins, extending to c. 75 m below paleosurface levels (Nijman et al., 1998; Ueno et al., 2008; Ueno, Isozaki, et al., 2001; Ueno, Maruyama, et al., 2001; Van Kranendonk et al., 2019). Coarsely crystalline barite also occurs throughout the North Pole Chert member. It occurs in veins transecting sedimentary layers, within bedded horizons where the barite crystals cut into sedimentary rocks and stromatolites, and atop hydrothermal veins as mound-shaped deposits (Baumgartner, Van Kranendonk, Fiorentini, et al., 2020; Djokic et al., 2017; Nijman et al., 1998; Van Kranendonk et al., 2003, 2006, 2008; Van Kranendonk & Pirajno, 2004).

The original model for the Dresser Formation proposed deposition in a quiet lagoonal environment (Buick et al., 1981; Buick & Dunlop, 1990; Groves et al., 1981; Walter et al., 1980), similar to Shark Bay in Western Australia, where stromatolites thrive in the intertidal zone of a quiet lagoonal setting (e.g., Jahnert & Collins, 2012). This model posits that the bedded barite in the North Pole Chert member originated as evaporative gypsum deposits that were later transformed into barite through hydrothermal overprinting (Buick & Dunlop, 1990). In contrast, more recent studies argue that the coarsely crystalline barite is a primary precipitate, associated with the emplacement of the hydrothermal veins that occurred synchronously with the deposition of the Dresser Formation (Nijman et al., 1998; Runnegar et al., 2001; Ueno et al., 2008; Van Kranendonk, 2006; Van Kranendonk et al., 2008; Van Kranendonk & Pirajno, 2004). This newer model, supported by studies on the geometry and inferred timing of vein emplacement, as well as the discovery of widespread barite-rich hydrothermal-depositional units (including putative fossiliferous hot spring fields), implies that life thrived in transient shallow-water to subaerial settings within a tectonically active, but infrequently eruptive, volcanic caldera basin with voluminous hydrothermal activity (Baumgartner et al., 2019; Baumgartner, Caruso, Fiorentini, et al., 2020; Baumgartner, Van Kranendonk, Fiorentini, et al., 2020; Baumgartner, van Kranendonk, Pagès, et al., 2020; Caruso et al., 2021; Djokic et al., 2017, 2021, 2024; Nijman et al., 1998; Van Kranendonk, 2006, 2011; Van Kranendonk et al., 2008; Van Kranendonk & Pirajno, 2004).

3 | METHODS

In 2019, drill cores SWA1A and SWA2 (Figure S1) were obtained using HQ (63.5 mm diameter) diamond drilling using water as a lubricant (see Appendix S1). The drill cores intersected relatively

unweathered pyritic stromatolites and stromatolitic structures within the North Pole Chert member. They are currently archived by the Geological Survey of Western Australia (GSWA), with identifiers M0003746 for SWA1A and M0003747 for SWA2.

Initial sampling was conducted at the University of New South Wales (UNSW; Kensington, NSW), where the drill cores were stored in cool, dry conditions. The selected materials were subsampled using clean band and rotary saws at the Mineral Resources section of the Commonwealth Scientific and Industrial Research Organisation (CSIRO; Kensington, WA). The resulting rock slabs were polished using distilled water and diamond micron polishing powder. One sample from drill core SWA2 was prepared as a polished thin section. The morphological and textural characterizations of the stromatolites and stromatolitic structures (Figure 1 and Figure S2) follow the terminology in Walter et al. (1992).

For stable isotope analyses of C and O in carbonate (see Appendix S1), several grams of powdered material were obtained from each sample using a clean diamond drill bit attached to a Dremel 4000 Rotary Tool. Elemental mapping on the polished core slabs was performed using Micro X-ray Fluorescence Microscopy analysis ("Maia Mapper"; see Appendix S1). Raman Spectroscopy and Scanning Electron Microscopy, including Backscattered Electron (BSE) and Secondary Electron (SE) imaging, as well as chemical analysis using Energy-Dispersive X-ray Spectroscopy (EDS), were conducted on the drill core slabs and thin sections (see Appendix S1).

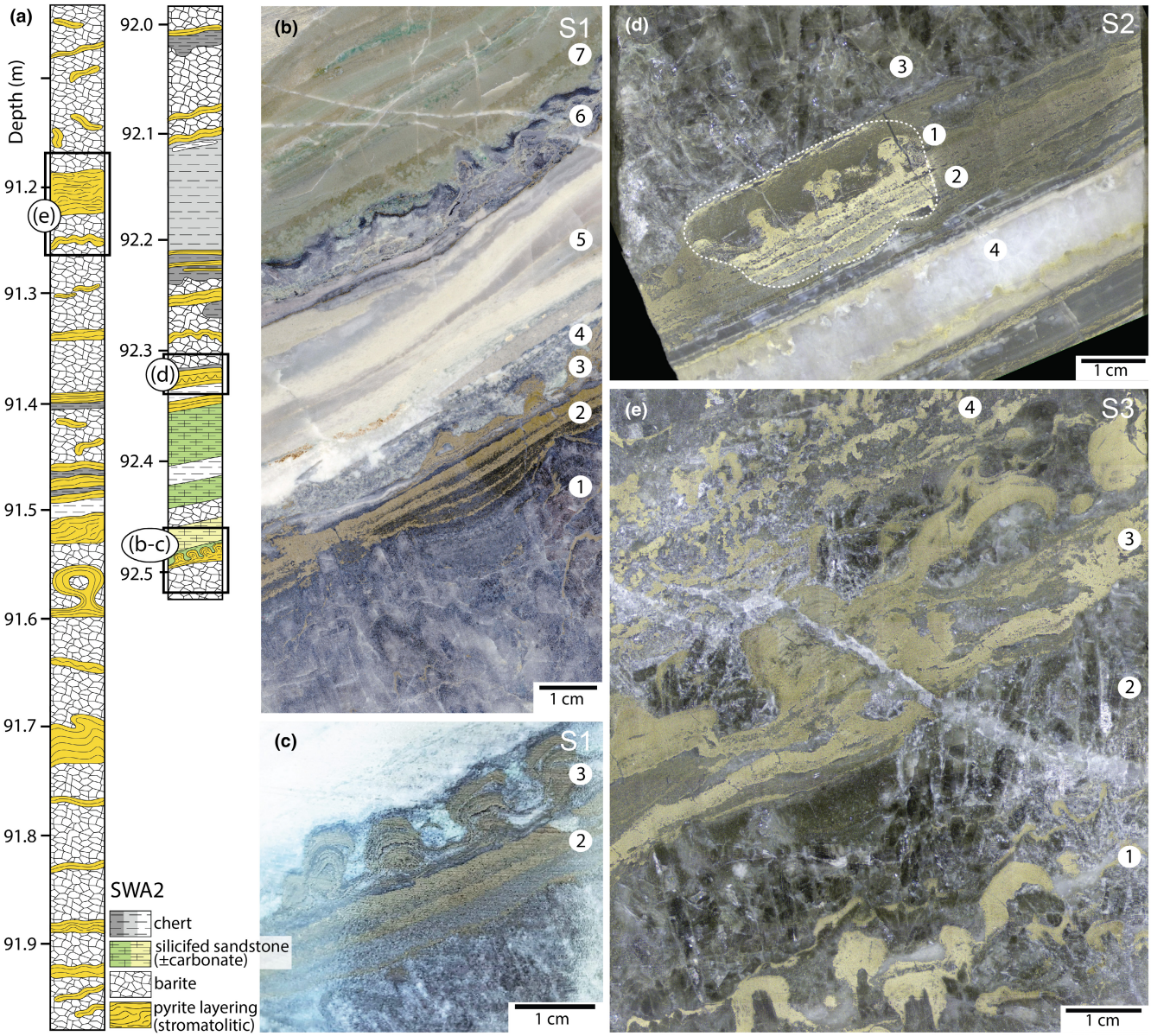

FIGURE 1 Lithological log of drillhole SWA2 (panel a) and photographs of samples S1-S3 (panels b-e). Panels (b, d, e) show rock slabs cut along the drill core axes (samples S1–S3, respectively). Panel (c) shows the core surface from which sample S1 was taken. The dashed line in panel (d) delineates the effects of nitric acid etching (see Section 3). Refer to the numbered circles and the main text for descriptions of lithological units and features.

The in-situ experiments were conducted both prior to and after localized etching of the sample surfaces with 70% ultrapure HNO_3. The acid was applied for c. 60–90 s under clean lab conditions, utilizing air displacement pipettes. It corroded pyrite and, to a lesser extent, carbonate, while OM remained largely unaffected (see also Baumgartner et al., 2019; Schieber, 2002). After flushing with distilled water, the samples were dried at c. 40–45°C in a clean laboratory oven, then transported and stored using clean desiccators or airtight plastic containers. Handling using vinyl/nitrile gloves minimized contamination. All analyses concluded within 1–2 weeks post-etching to ensure the examination of surfaces free from atmospheric oxidation.

4 | RESULTS

Rock slabs collected from two drill cores through the North Pole Chert member (SWA1A and SWA2; Figure S1) contain morphologically diverse stromatolites and stromatolitic laminae, primarily composed of pyrite. These structures occur within strata variably influenced by syn- and post-depositional hydrothermal activity (Figure 1 and Figure S2; cf. Van Kranendonk et al., 2008).

4.1 | Morphology, texture, and host rock characteristics

Morphology, texture, and host rock characteristics were examined in samples S1–S3 from drill cores SWA2 (Figure 1) and samples S4 and S5 from SWA1A (Figure S2). Primary investigations focussed on samples S1–S3, which comprise a wide range of lithologies and morphologically diverse stromatolites and stromatolitic structures. Detailed information about samples S4 and S5, displaying features similar to those in samples S1–S3, is available in Appendix S1.

Sample S1 was collected from 92.5 m in drillhole SWA2 (Figure 1a). Its base features a layer of upward-pointing barite crystals (indicated as 1 in Figure 1b), several centimeters thick, which intrude into a c. 2 cm thick sedimentary unit containing stromatolites. This unit consists of flat-laminated pyrite (2 in Figure 1b), overlain by undulatory and pseudocolumnar structures with wavy to wrinkly laminations, and also distinctly columnar to domal (bulbous to nodular) structures displaying convex-upward laminations (3 in Figure 1b; Figures 1c, 2a, 3a). The laminae within the columnar to domal structures thicken at the crests, turn down sharply, are truncated at the margins, or bridge across to the adjacent structures (Figure 1c). Elemental mapping shows strong signals of Ca in the host strata (Figure 3b), reflecting dolomite-ankerite carbonate (additional details are provided in Section 4.2). Compared with the basal stratiform pyrite (2 in Figure 1b), the stromatolites (3 in Figure 1b,c) exhibit higher Ni but lower As concentrations (Figure 3c,d). These stromatolites are covered by a fine-grained sandstone devoid of pyrite – a similar sandstone occurs in sample S4 (see Figure S4). This sandstone contains angular to subangular felsic volcanic glass shards and subangular spinel grains within a matrix replaced by silica and carbonate (Figure 2b,c). These spinel grains are (Al-) chromites with a wide range of compositions akin to those in basalts and komatiites (Figure S3), suggesting derivation of heterogeneous detritus from across a wide area. Above the sandstone lies c. 2–3 cm thick chert interlayered with yellow carbonate (5 in Figure 1b). Elemental mapping reveals Fe enrichments with only few Ca hotspots (Figure 3b), indicating that this carbonate is mostly siderite. This unit is overlain by thin (c. 1 cm) siliceous sediment interspersed with barite crystals and sphalerite stringers (6 in Figure 1b). The barite crystals cut into the base of overlying green, finely bedded chert (7 in Figure 1b).

Sample S2, located at 92.3 m in drillhole SWA2 (Figure 1a), comprises a c. 1 cm thick thinly bedded chert-carbonate. This unit features columnar pyritic structures, ranging from turbinate to incipiently branching (1 in Figure 1d), which overlie stratiform, flat-laminated to slightly undulatory pyrite with fine-grained carbonate (2 in Figure 1d). These intervals are capped by a several cm-thick layer of coarsely crystalline barite (3 in Figure 1d) and underlain by a sheet of post-depositional quartz plus siderite (4 in Figure 1d). Elemental mapping reveals chemical and mineralogical differences between the columnar structures and the underlying stratiform pyrite (Figure 4a,b). The latter shows lower Ni but a higher Ca level due to the presence of dolomite-ankerite matrix carbonate. Additionally, elemental mapping reveals that the equidistantly spaced (c. 1 cm apart) columns control the slightly wavy cross-stratification in the sediment between the columns (Figure 4b,c). For example, the infills on one side of the columns can exhibit an upward-grading pattern, from poorly sorted sediment at the bases to finely laminated sediment at the crests (1 in Figure 4d). Onlaps of fine-scale pyritic laminates onto the crests are observable (2 in Figure 4d). The opposite flanks can display gently dipping bedding (3 in Figure 4d), occasionally with wrinkly laminae propagating from the tops of the columns (4 in Figure 4d).

Sample S3 is derived from 91.2 m in drillhole SWA2 (Figure 1a). Its lower stromatolitic interval features deformed and dismembered pyritic laminae within coarsely crystalline barite and lesser chert-carbonate (1 in Figure 1e). Separated by a thick layer of coarsely crystalline barite with less sphalerite (2 in Figure 1e), the center of the sample contains c. 2–3 cm thick chert-carbonate with stromatolitic structures. These structures exhibit undulatory to columnar-layered or cumulative morphologies with wavy and wrinkly laminations, and are associated with patches of coarsely crystalline barite (3 in Figure 1e). Occasionally, broad columnar structures are characterized by fine-scale lamination that is generally uniform in thickness and curves upward in a convex manner (Figure 5a–c). The uppermost horizon consists of several cm thick coarse-grained barite with irregular pyrite (4 in Figure 1e). Elemental mapping reveals enrichments of Ni and As in the pyritic laminates within the two stromatolitic intervals (1 and 3 in Figure 1e), with variations delineating lamination and growth stages (Figure 5a–c). The signals of Ca relate to carbonate (dolomite-ankerite solid-solution series carbonate; Figure 5a and see Section 4.2). Layers of zoned barite

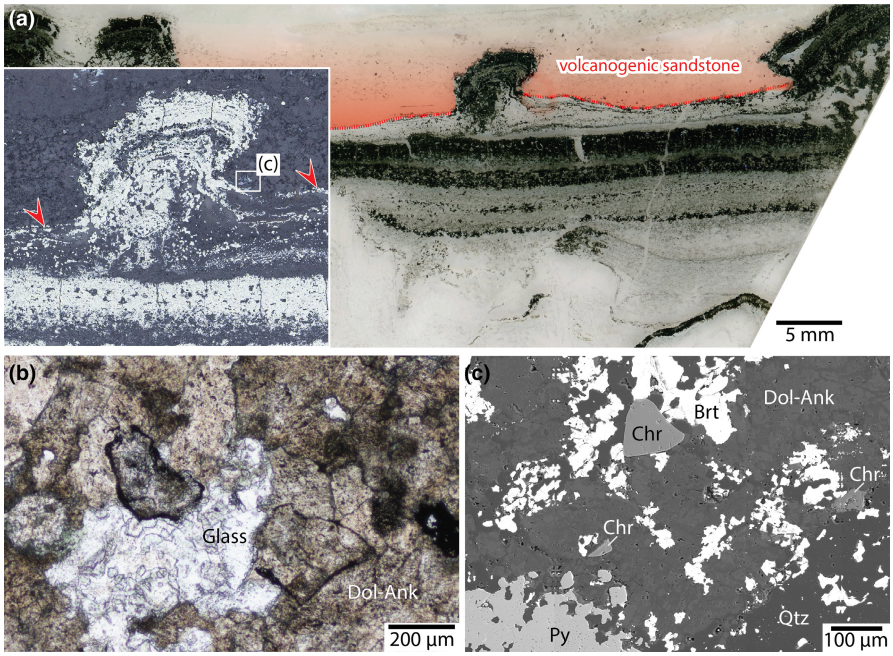

FIGURE 2 Petrography and mineralogy of stromatolites and their host strata in sample S1. (a) Overview photograph and reflected light microscopy image (inset), showing columnar stromatolites with convex-upward, wavy to wrinkly internal laminations, atop stratiform pyrite. Red indicates volcanic sandstone draped over the stromatolites. Red arrows in the inset point to the boundary between the columnar structure and the overlying sandstone. See Figure 7d for a map of OM. (b) Transmitted light microscopy image of glass shards and carbonate. (c) BSE image of spinel grains (see Figure S3 for chemical analyses and mineralogical classification). Brt, barite; Chr, chromite; Dol-Ank, dolomite-ankerite carbonate; Glass, volcanic glass; Qtz, quartz.

crystals, characterized by upward increases in Sr concentration, occur adjacent to or interleaved with the laminae (Figure 5a,b). In the lower part of the sample (1 in Figure 1e), Ni- and/or As-rich pyritic laminae are linked to discrete, bedding-parallel intervals of coarsely crystalline barite. Some barite crystals have pushed up, plastically deformed, or transected the pyritic laminae (Figure 5d,e). Consequently, the pyritic laminates at the tips of the barite crystals can show a uniform thickness at the top and sides (Figure 5d,e). This contrasts with bona fide columnar and domal stromatolites, whose lamination typically thickens at the crests (Figures 1c and 2a). Deformation is also evident in the center of this sample (3 in Figure 1e), where pyritic laminae within chert-carbonate and bedded microcrystalline barite strata are penetrated by the Sr-rich tips of barite crystals (Figure 5f,g). Similar features, with barite crystals intruding microcrystalline barite strata and pyritic laminae, are observable in sample S5 (see Figure S5).

4.2 | Petrography, mineralogy, and organic matter

Electron imaging and Raman Spectroscopy reveal that the pyritic structures consist predominantly of pyrite and barite organomineralization, alongside lesser amounts of quartz, barite, and carbonate. Specifically, their interiors are predominantly composed of nanoporous pyrite and, to a lesser extent, microspherulitic barite, with significant quantities of OM – see the details below, Figures 6 and 7 and Figure S6, as well as Baumgartner et al. (2019, their figure 2) and Baumgartner, Van Kranendonk, Fiorentini, et al. (2020, their figure 3).

Consistent with Baumgartner et al. (2019), nanoporous pyrite is the main mineral-organic assemblage, regardless of variations in host lithology and stromatolite morphology (e.g., columnar or domal versus stratiform forms; see Section 4.1). Electron imaging after nitric acid etching revealed the distribution of OM. It occurs as dispersed aggregates within nanoporosity (Figure 6b,c), and as larger, irregular, or small sheath-like accumulations that can pass through pyrite grain boundaries (Figure 6d–i). As reported in Baumgartner, Van Kranendonk, Fiorentini, et al. (2020), the nanoporous pyrite co-occurs with microspherulitic barite. It appears as: (i) clusters of numerous microscopic aggregates alongside OM (see Figure 6j,k and Baumgartner, Van Kranendonk, Fiorentini, et al., 2020, their figure 3); and (ii) agglomerations pseudomorphed by pyrite, containing less OM than the primary aggregates (see Figure 6l–n and Baumgartner, Van Kranendonk, Fiorentini, et al., 2020, their figure 4). Determining the exact proportions of microspherulitic barite is challenging, as this requires electron imaging at lower micron to sub-micron scales following acid etching. Nevertheless, estimates indicate that the stromatolites in samples S1 and S2 contain less microspherulitic barite than the stromatolitic structures in samples S3–S5, mirroring the respective proportions of coarsely crystalline barite in the host strata (Figures 4 and 5, Figures S4 and S5). Specifically, in samples S1 and S2, the microspherulitic barite, though mostly pseudomorphosed into pyrite (Figure 6l–m), locally reaches up to c. 20% by volume. In contrast, the structures in samples S3 and S5 contain up to ≥50% in certain areas.

Raman Spectroscopy analysis shows that the OM spectra from all samples exhibit minor variations (Figure 7 and Figure S6), with two prominent peaks at c. 1345 cm^{-1} and c. 1610 cm^{-1} (Figure 7a,b and Figure S6a) identified as the disorder-induced "D band" and order-induced "G band", respectively. A representative OM spectrum has been fitted using pseudo-Voigt functions (D1 at c. 1345 cm^{-1}, D2 at c. 1615 cm^{-1}, D3 at c. 1510 cm^{-1}, D4 at c. 1250 cm^{-1}, and G* at c. 1590 cm^{-1}), based on the carbonaceous

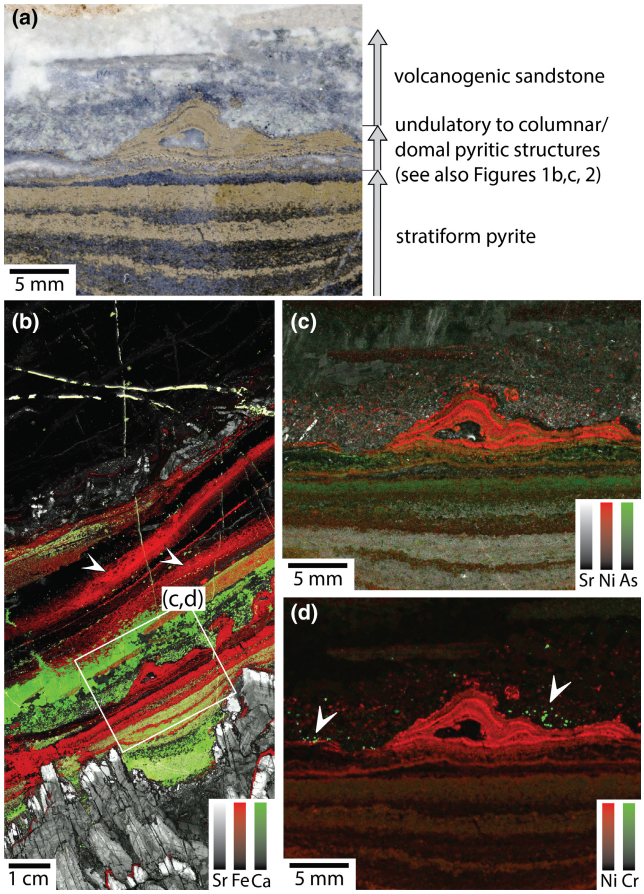

FIGURE 3 Elemental maps and characterization of stromatolites in sample S1. (a) Photograph showcasing the transition between stratiform pyrite and overlying, undulatory to pseudocolumnar structures with wavy to wrinkly lamination. The latter domain also comprises columnar to domal structures (Figures 1c, 2a, 7c,d). Volcanic sandstone containing (Al-) chromite grains overlies and fills the spaces between the pyritic structures [see panel (d) and Figure 2]. (b–d) Maps of Sr, Ca, Fe, Ni, As, and Cr, with Ca signals related to carbonate (dolomite-ankerite; see Section 4.2 and Figure 8) and Sr in panel (b) indicating zoned barite crystals. In panel (b), Fe relates to pyrite in stromatolites, and ferrous carbonate, mainly siderite, in the overlying chert-carbonate unit (indicated by arrows). In panels (c, d), Ni and As are concentrated in pyrite, while Cr in panel (d) indicates chromite (arrows).

matter geothermometer in Kouketsu et al. (2014). The shape of the spectrum and the full width at half maximum (FWHM) of the D1 and D2 bands (c. 98 cm^{-1} and c. 38 cm^{-1}, respectively; Figure 7b) indicate c. 270–280°C thermal maturity. This value is slightly lower than previous estimates for the OM in the pyritic Dresser stromatolites (Baumgartner, van Kranendonk, Pagès, et al., 2020), due to the more precise application of the Kouketsu et al. (2014) geothermometer. Raman Spectroscopy mapping reveals ubiquitous enrichments of OM within the pyritic structures. In sample S1, a scan across a columnar stromatolite structure shows significant amounts of pyrite-hosted OM (Figure 7c,d). Data from sample S2 trace the distribution of nanoporous pyrite and OM in both the columnar stromatolites and the underlying stratiform pyrite (Figure S6b,c). Similarly, strong enrichments of OM occur in the pyritic structures of samples S3–S5 (Figure S6d–i).

The nanoporous pyrite-microspherulitic barite assemblages are generally overgrown by nonporous pyrite rinds devoid of OM (Figure 8 and Figure S7). In pyritic structures within cherty sequences lacking large barite crystals (e.g., sample S2), this outer pyrite is often overgrown by carbonate, especially Fe-rich dolomite and minor ankerite enriched in Mn [dolomite-ankerite solid-solution series; $Ca(Mg,Fe,Mn)(CO_3)_2$]. This carbonate is distinct from the accessory, finer grained siderite-rhodochrosite solid-solution series carbonate [dominantly Mn-bearing siderite; $(Fe,Mn)CO_3$] associated with nanoporous pyrite within the pyritic structures (Figures 6g,l and 8 and Figure S7). In barite-rich sequences of samples S3 and S5, this outer pyrite is often lined by micaceous assemblages (Figure S8a,b), comprising muscovite-paragonite solid-solution series mica [$(Na,K)Al_2(AlSi_3O_{10})(OH)_2$] and Mg-Fe-Al-rich phyllosilicates, likely chlorite [$(Mg,Fe)_2Al_3(AlSi_3O_{10})(OH)_8$; Figure S8c].

4.3 | Carbon and oxygen isotopes in carbonate

Figure 9 presents the C and O stable isotope data ($\delta^{13}C_{carb}$ and $\delta^{18}O_{carb}$) for carbonates within the stromatolite/stromatolitic intervals of samples S2 and S3 (1 and 2 in Figures 1d and 3 in Figure 1e), as well as for the bedded siderite in sample S4 (4 in Figure S2b). In samples S2 and S3, $\delta^{13}C_{carb}$ values ranging from c. −4‰ to −2‰ reflect the groundmass dolomite-ankerite carbonate, which dominates over the Mn-bearing siderite within the pyritic laminates (see Section 4.2). The bedded siderite in sample S4 shows a $\delta^{13}C_{carb}$ value of c. −0.5‰ (Figure 9). Negative $\delta^{18}O_{carb}$ values are observed for all carbonate generations; c. −10‰ to −13‰ for the dolomite-ankerite carbonate in samples S2 and S3, and c. −13‰ to −15‰ for the bedded siderite in sample S4. Collectively, these data illustrate a slightly negative correlation between $\delta^{13}C_{carb}$ and $\delta^{18}O_{carb}$ (Figure 9).

4.4 | Organic filamentous microstructures

The opacity of pyrite hinders the examination of enclosed OM using transmitted light microscopy. Therefore, nitric acid etching was used to dissolve the pyrite, exposing not only irregular OM aggregates (Figure 6d–i) but also as complexly textured organic microstructures. These include filamentous, cylindrical to tubular, and intricate sheath-like forms (see Figure 10 and refer for to Baumgartner et al., 2019, their figure 4). Figure 10a–d shows a microfilament emerging from nanoporous pyrite beneath quartz. It transitions into a tubular sheath structure, characterized by striated ends and frayed strands that grade at the edges into clotted OM particles (Figure 10b). The microfilaments in Figure 10e,f have retained a partially pyritic composition after nitric acid etching. Specifically, the microfilament in Figure 10e exhibits characteristics of a frayed tubular structure with multiple aligned

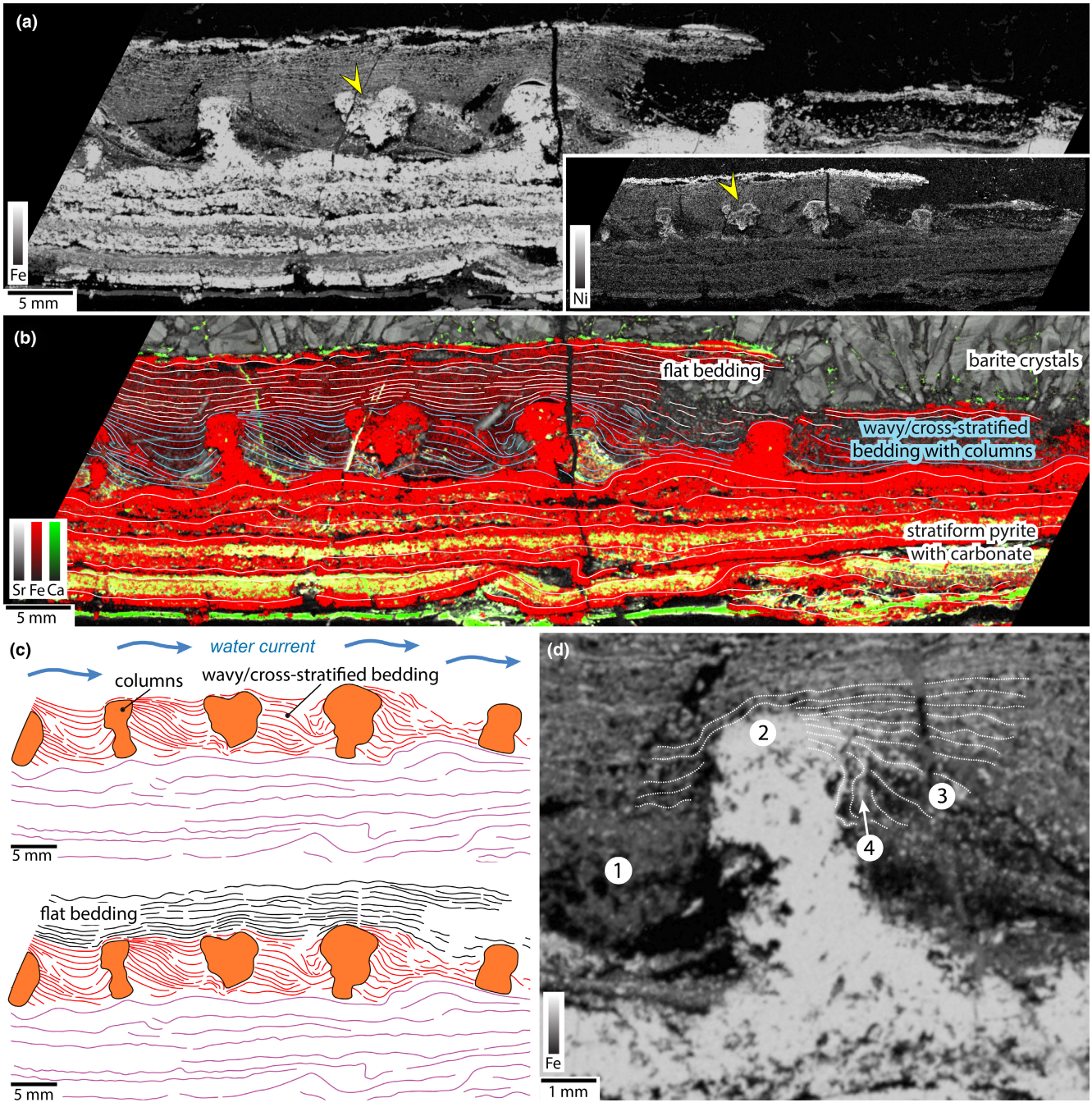

FIGURE 4 Elemental maps and characterization of stromatolites in sample S2. (a, b) Maps of Sr, Fe, Ni, and Ca. The Fe and Ni signals mostly indicate pyrite within the stromatolites, whereas Ca and Sr relate to carbonate and barite, respectively. The mm-scale, locally branching columns [arrows in panel (a)] show consistent spacing. They determine the geometry of irregular wavy, cross-stratified bedding [cyan lines in panel (b)], and are overlain by a flat, finely bedded stratum. (c) Illustration of stromatolites and their relationships with depositional textures. (d) Map of Fe in a pyritic column. The indicated features (1–4) are described in Sections 4.1 and 5.2. See Figure S6b,c for a BSE image and a Raman spectroscopy map of OM.

nanostrands. Figure 10g–j shows partially pyritic filamentous microstructures that traverse grain boundaries and transition from a smooth, sheath-like, filamentous morphology to frayed, ropey microstrands. Raman Spectroscopy confirms the high thermal maturity of the OM in the filamentous microstructures, equivalent to that of the surrounding OM (see Figure 10k and Section 4.2 for a thermal maturity estimation).

5 | DISCUSSION

5.1 | Concepts in assessing stromatolite biogenicity

Determining the origins of ancient stromatolites and distinguishing between the biological and non-biological (physical depositional) processes in their formation is challenging. Stromatolites

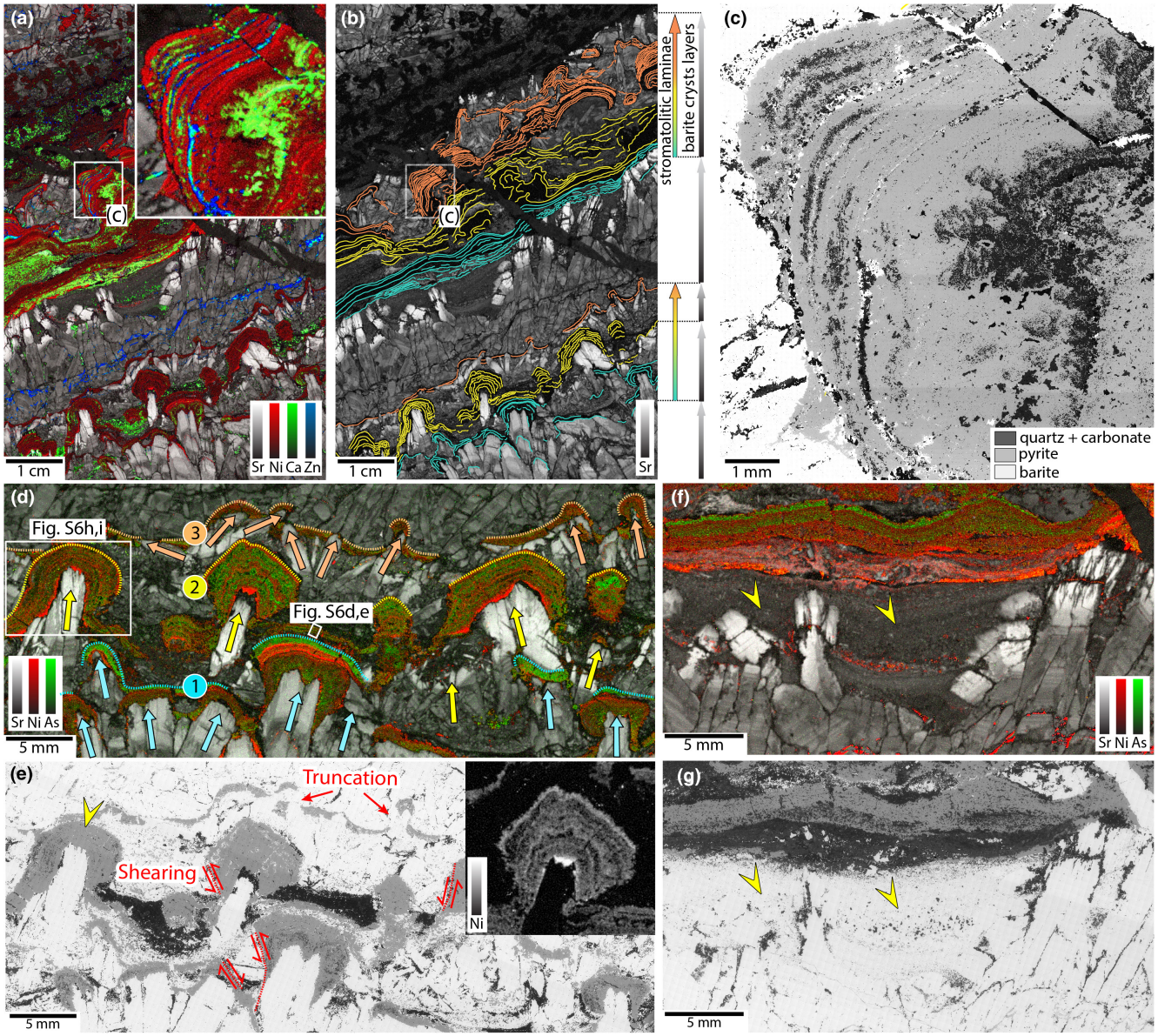

FIGURE 5 Elemental maps and characterization of stromatolitic structures in sample S3. (a, b) Maps of Sr, Ni, Ca, and Zn. Nickel and Zn indicate pyrite and sphalerite, respectively. Calcium and Sr relate to carbonate and barite, respectively. Inset in panel (a) shows a broad columnar structure with internal lamination delineated by Ni. Indicated in panel (b) are two stromatolitic domains (coloured arrows) and beds of barite crystals (grey arrows). (c) BSE image of the columnar structure indicated in panel (a). Mineralogy is inferred from brightness differences. (d–g) Elemental maps (Sr, Ni, and As) and BSE images of the pyritic laminae and host strata. Panels (d, e) show pyritic layers (indicated by Ni and As) interleaved with barite crystals [numbered lines and coloured arrows in panel (d)]. Red in panel (e) indicates deformation features (shearing and truncation) caused by the barite crystals. Yellow arrow indicates a pyritic layer at the tip of a large barite crystal that exhibits a (near-) uniform thickness at the top and sides. The Ni map in panel (e) reveals fine-scale lamination within pyrite at the tip of a barite crystal. Panels (f, g) display chert-carbonate-hosted laminae lying above bedded stratum dominated by microcrystalline barite (indicated by arrows).

exhibit distinctive lamination enriched in OM (Kalkowsky, 1908), which appears smooth, wavy, or wrinkly, and typically develops in convex-upwards direction. Hence, morphology and texture are key indicators for identifying stromatolites (e.g., Allwood et al., 2006, 2009; Awramik & Grey, 2005; Baumgartner et al., 2019; Buick et al., 1981; Grey & Awramik, 2020; Hofmann et al., 1999; Van Kranendonk, 2006, 2011; Van Kranendonk et al., 2008; Walter et al., 1980). However, these characteristics are often considered unreliable because abiological processes can form structures that mimic stromatolites (e.g., Grotzinger & Knoll, 1999; Grotzinger & Rothman, 1996; McLoughlin et al., 2008; Neveu et al., 2018). This raises a fundamental question: beyond morphology and texture, what additional characteristics can help distinguish stromatolites from abiotic mimics?

The original definition describes stromatolites as "organogenic, laminated calcareous rock structures, the origin of which is

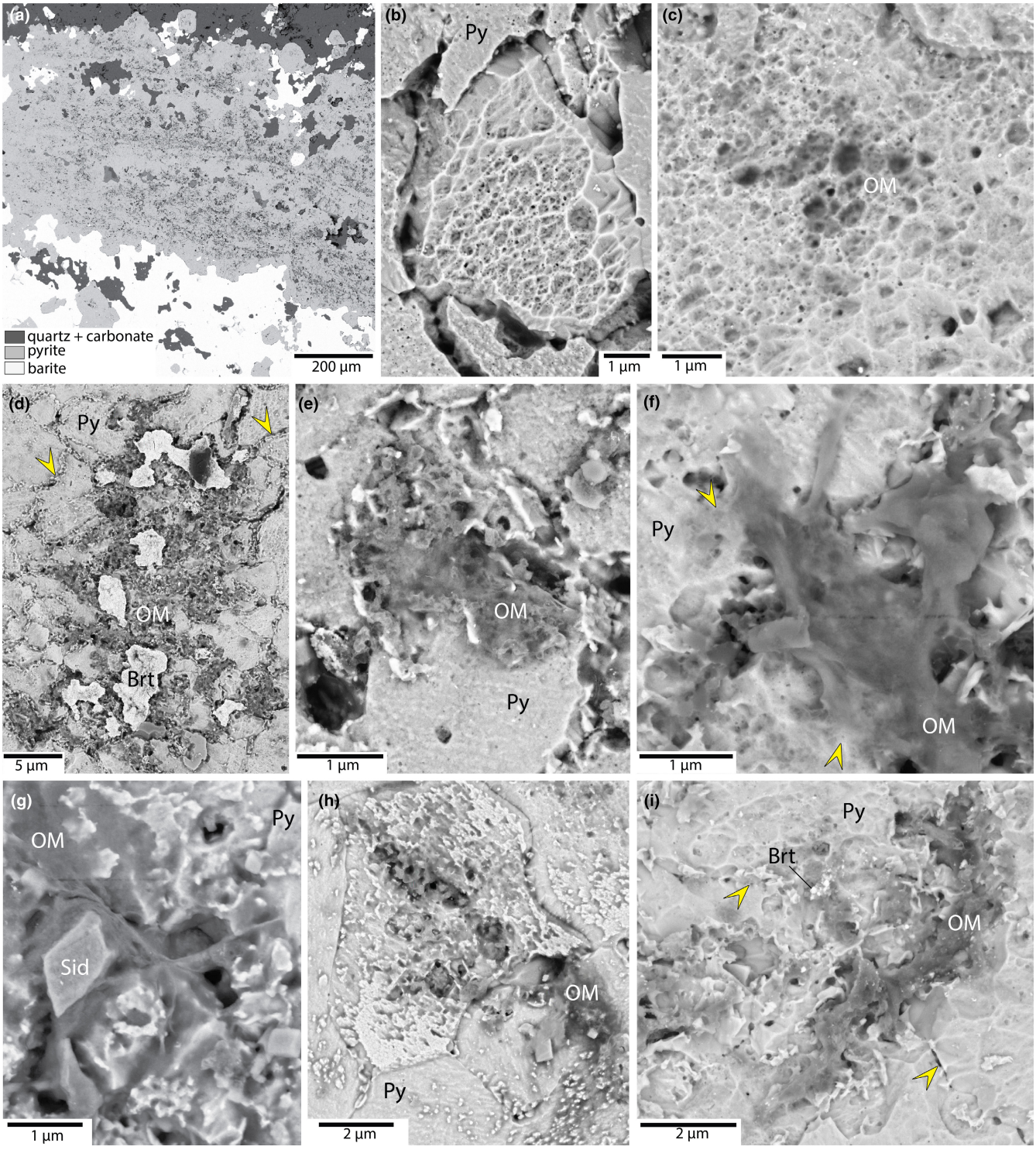

FIGURE 6 Mineral-organic assemblages observed after nitric acid etching of pyrite. (a) BSE image of a pyritic lamina (sample S3) hosted within barite (bottom) and chert-carbonate (top). Mineralogy is determined from brightness differences. (b, c) Nanoporous pyrite with OM [grey substance in pores in panel (c)]. (d) Accumulations of OM associated with nanoporous pyrite and barite. Arrows indicate pyrite grain boundaries. (e, g) Irregular sheath-like OM. Arrows in panel (f) indicate OM emanating from nanoporous pyrite. Note the siderite grain in panel (g). (h, i) Irregular OM passing across grain boundaries [arrows in panel (i)]. (j, k) Microspherulitic barite plus OM [grey substance between the spherules; panel (k)]. (l–n) Microspherulitic barite pseudomorphosed to pyrite (samples S2 and S5). Note the siderite grain in panel (l) and the relict OM in panel (*n*). Brt*, microspherulitic pyrite pseudomorphs after barite [panels (l–n)]; Brt, microspherulitic barite; Phyl, unspecified phyllosilicates; Py, pyrite; Qtz, quartz; Sid, siderite.

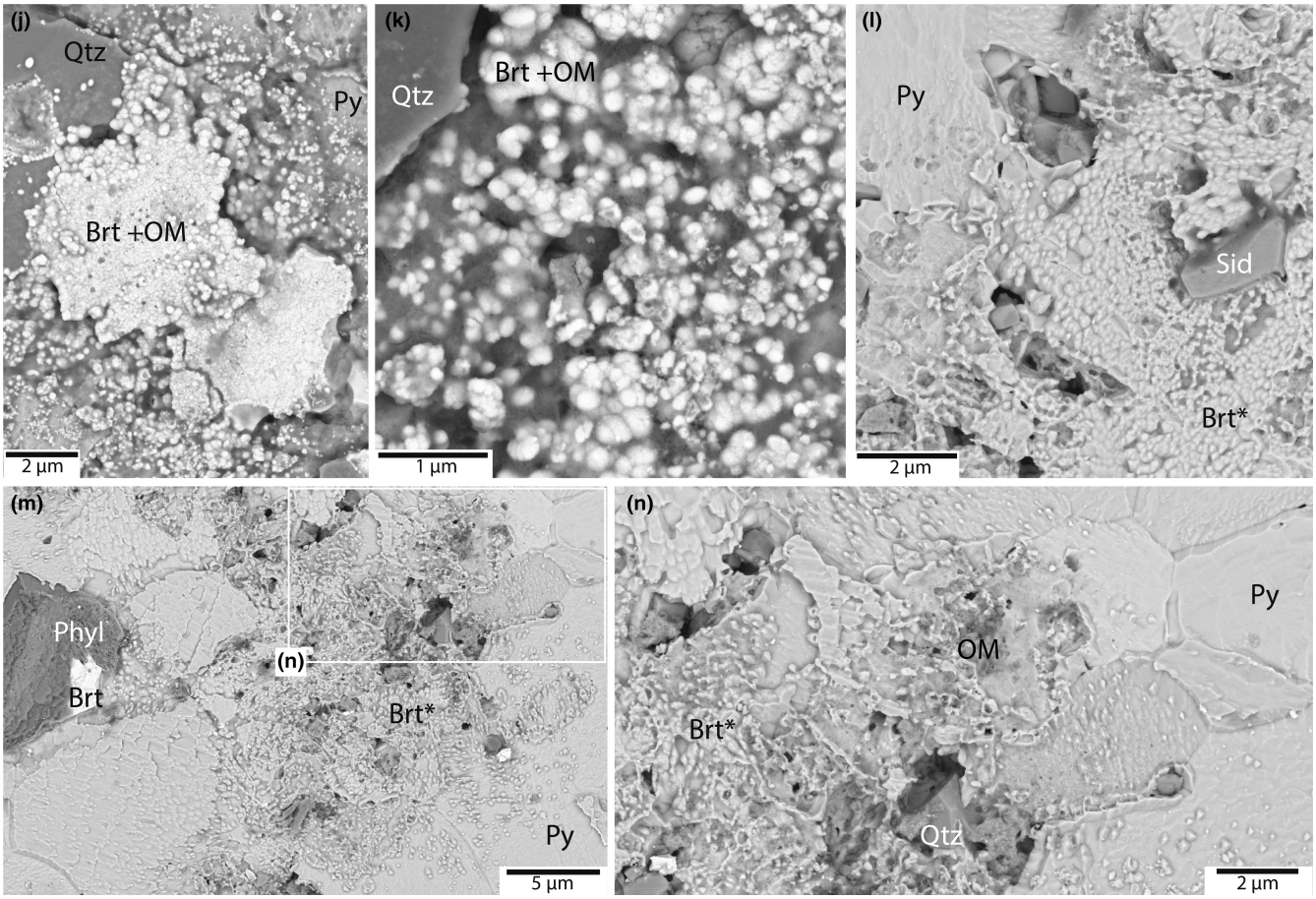

FIGURE 6 (Continued)

clearly related to microscopic life, which in itself must not be fossilized (Kalkowsky, 1908; translated by Krumbein, 1983)". Many attempts have since been made to refine this terminology (cf. Grey & Awramik, 2020). For instance, Semikhatov et al. (1979) proposed a purely morphological description: "an attached, laminated, lithified sedimentary growth structure accreting away from a point or limited surface of initiation". Walter (1976) proposed a biogenic definition: "organosedimentary structures produced by sediment trapping, binding and/or precipitation due to the growth and metabolic activities of microorganisms". However, ongoing debates revolve around whether stromatolites should contain discernible microbial remnants, such as degraded microbial biomass or residual EPS, or even distinct microfossils.

Buick et al. (1981) proposed a hierarchical set of criteria for assessing biogenicity: (i) stromatolites should demonstrate syngenetic relationships with their (meta-) sedimentary host strata; (ii) they should exhibit convex-upwards morphologies with curved, wavy or wrinkly lamination that thickens over flexure crests; and (iii) microfossils should be present, preferably in ways indicating mineral precipitation and sediment trapping/binding induced by living microorganisms, and with correlations between contrasting microfossil assemblages and differences in stromatolite morphology (Cloud & Morrison, 1979). However, criterion (iii) might exclude biogenicity for most, if not all, Archean stromatolites, as preserved microfossils, let alone diverse microfossil assemblages, are commonly absent (e.g., Lepot, 2020).

In this study, we investigate four points of supporting evidence for biogenicity, taking into account the well-preserved depositional context and the composition of the pyritic Dresser stromatolites:

(i) Stromatolites should exhibit distinctive morphologies and textures that contrast with non-biological depositional textures in the host strata.
(ii) Following point (i), there should be evidence of syn-depositional sediment accumulation and/or mineral precipitation, distinctly highlighting the interplay between microbial activity and depositional processes.
(iii) Significant quantities of OM should be present, demonstrated not to have been introduced by later processes, and exhibiting a thermal maturity that is consistent with the thermal alteration of the host rock.
(iv) To support point (iii), the OM should be an integral component, hosted by distinctive mineral-organic assemblages that are distinguishable from later mineralization processes.

Supporting evidence (i) emphasizes the importance of distinctive morphologies and textures that, when contrasted with the

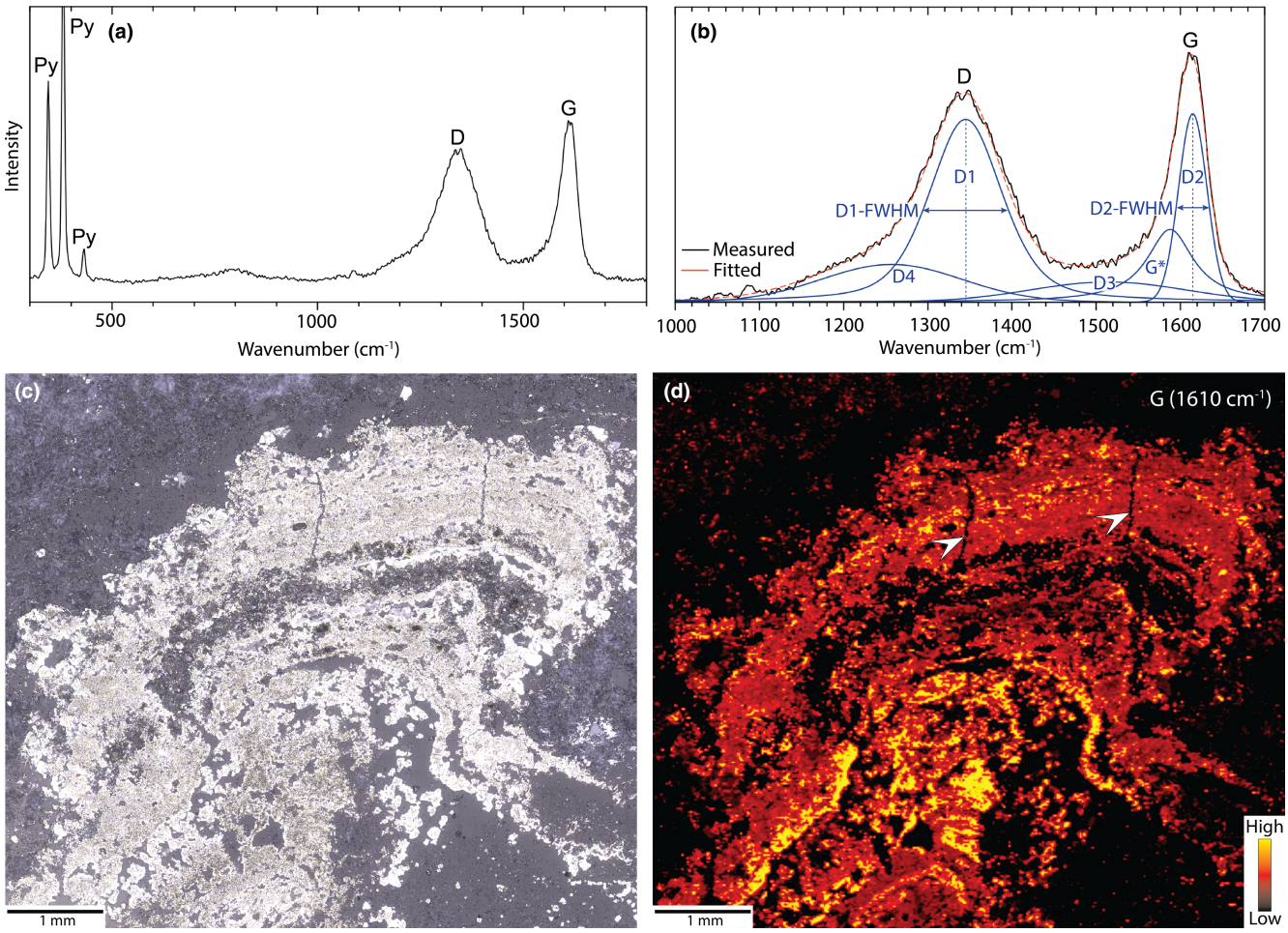

FIGURE 7 Raman spectroscopy analysis of OM within a pyritic columnar structure in sample S1. (a) Spectrum of OM (300–1800 cm^{-1}) with bands of pyrite (Py) and OM (D at c. 1345 cm^{-1} and G at c. 1610 cm^{-1}). (b) Mathematical deconvolution of the 1000–1700 cm^{-1} range using pseudo-Voigt profiles (D1, D2, D3, D4, and G*), according to Kouketsu et al. (2014). Thermal maturity is estimated based on FWHM of the D1 and D2 bands (c. 98 cm^{-1} and 38 cm^{-1}, respectively). (c, d) Reflected light image and scan of OM after nitric acid etching. Arrows indicate quartz-filled fractures/fissures devoid of OM.

host sediment, cannot be attributed to abiotic processes. This premise considers that stromatolites, even when found in ancient deposits, can retain textural and compositional characteristics that markedly differ from the host strata (e.g., Van Kranendonk, 2011, Van Kranendonk et al., 2019). Hence, biological and abiological processes can be shown to have operated simultaneously, with interference textures tracing interplays between microbial activity and depositional processes [supporting evidence (ii)]. Identifying such relationships helps demonstrating biogenicity, as suggested for the Dresser Formation and other fossiliferous units in the Pilbara Craton (e.g., Van Kranendonk, 2011; Van Kranendonk et al., 2019).

Adopting this approach instils confidence in discerning stromatolites from potential abiological mimics, including the mineral crusts described by Grotzinger and Rothman (1996). Additionally, caution is warranted when generalizing results from laboratory experiments. For instance, the relevance of the "abiogenic spray paint stromatolitic structures" reported by McLoughlin et al. (2008), formed by colloidal particle deposition under specific physicochemical conditions induced by high-velocity particle stream impacts, has yet to be demonstrated in natural settings. While windblown or steam-driven processes can be conceived, there is no relevance to the shallow-water environments typical of stromatolite formation, which are characterized by distinctive fluid flow regimes and physical-sedimentological factors (see Sections 5.2, 5.4, and 5.5).

Another challenge arises from mathematical models for the abiotic formation of stromatolitic structures (e.g., Grotzinger & Rothman, 1996). However, these models oversimplify the numerous factors and uncertainties inherent in natural systems. For example, Grotzinger and Rothman (1996) modeled the growth of stromatolitic structures using only four simplified variables: (i) sediment fallout; (ii) diffuse smoothing of sediment and surface tension in chemical precipitation; (iii) surface-normal precipitation, and (iv) surface heterogeneity and environmental fluctuations represented by random noise. Furthermore, the equations used to describe stromatolite growth are contested (Batchelor et al., 2003). These considerations underscore that mathematical models cannot replace or be used to

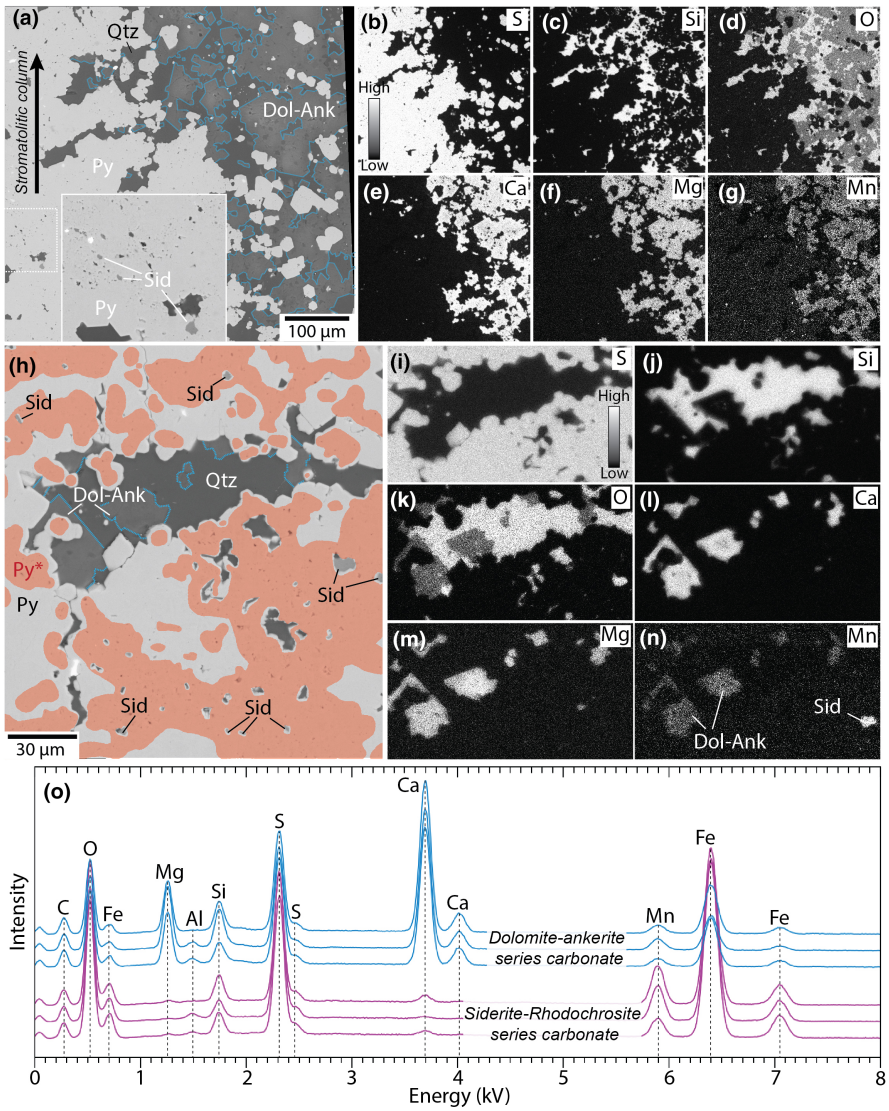

FIGURE 8 Carbonate associated with a pyritic column in sample S2. (a) BSE image of Mn-bearing dolomite-ankerite carbonate (blue lines) adjacent to the pyritic column. The inset shows Mn-bearing siderite within pyrite. (b–g) EDS elemental maps (S, Si, O, Ca, Mg, and Mn) of the area in panel (a). (h) Mn-bearing siderite within nanoporous pyrite (indicated in red). Dolomite-ankerite carbonate is restricted to the host stratum [see also panel (a)]. (i–n) Elemental maps of the middle area in panel (h). (o) EDS spectra of carbonates. The high counts of S and Fe are due to signals from pyrite during EDS analysis in the low-vacuum mode without C coating. DolDol-Ank, dolomite-ankerite carbonate; Py*, nanoporous pyrite; Py, pyrite; Qtz, quartz; Sid, Mn-bearing siderite.

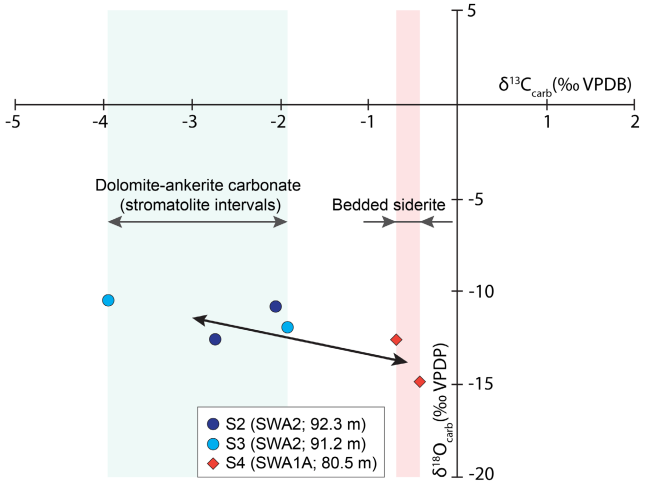

FIGURE 9 Carbon and O isotope ($\delta^{13}C_{carb}$ and $\delta^{18}O_{carb}$) composition of carbonates. Arrow indicates the isotopic signature difference between the dolomite-ankerite carbonate in fossiliferous intervals (samples S2 and S3) and the bedded siderite in sample S4.

dismiss direct evidence, especially when it is grounded in a clear understanding of the conditions under which a structure in question formed (see Sections 5.2, 5.4, and 5.5).

Supporting evidence (iii) and (iv) provide support for microbial origins by showing that the OM is integral to the structures, rather than a result of unrelated processes like post-depositional hydrocarbon migration. Focusing on demonstrably autochthonous OM, especially when it displays additional characteristics indicative of decomposed microbial remnants, alleviates the need for preserved microfossils, which are typically absent in Archean stromatolites. This approach also reduces the risk of confusion with abiotic biomorphs (e.g., Cosmidis & Templeton, 2016; Nims et al., 2021). While supporting evidence (i) and (ii) apply to stromatolites of all ages, the broader significance of points (iii) and (iv) remains to be fully explored. While Archean stromatolites typically lack significant OM, the pyritic Dresser stromatolites have been shown to contain high concentrations of thermally mature OM, displaying characteristics indicative of microbial remnants (Baumgartner et al., 2019).

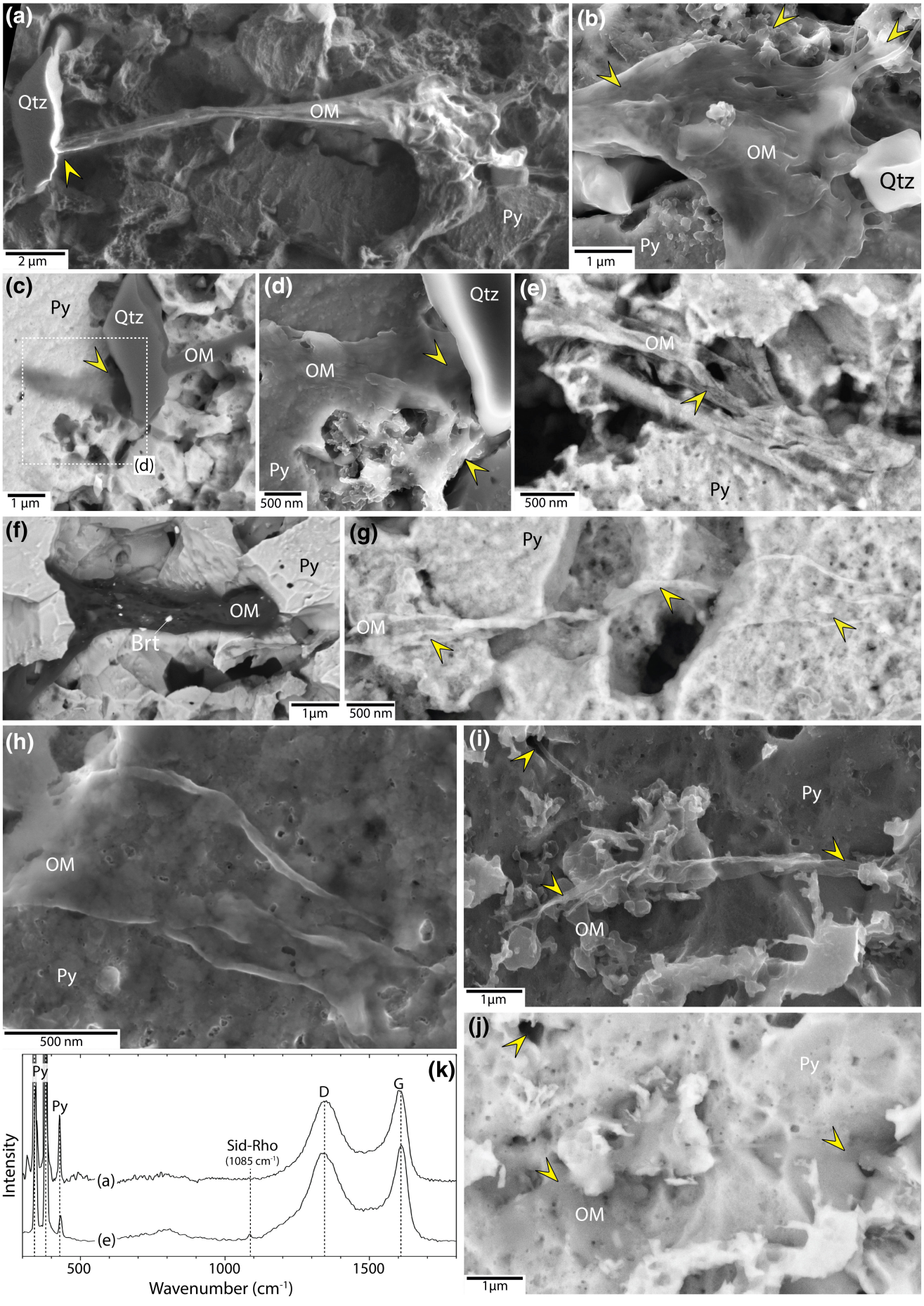

FIGURE 10 Filamentous organic microstructures observed within nanoporous pyrite after nitric acid etching. (a, b) Secondary electron (SE) images of a tubular filamentous sheath. Arrow in panel (a) indicates the location where it delves beneath quartz. Lower arrow in panel (b) indicates the torn opening, while the upper arrows indicate strands and organic nanoparticles. The images in the inset and panels (b–d) were acquired after C coating. (c, d) Detailed SE and BSE images of the organic structure in panels (a, b). Arrow in panel (c) and upper arrow in panel (d) indicate the location where the filament emerges from beneath quartz. Lower arrow in panel (d) indicates strands transitioning into organic nanoparticles. (e–h) BSE and SE images of filamentous OM. Panels (e, f) show cylindrical microstructures with multiple strands [arrow in panel (e)]. Their partially pyritic composition is indicated by high brightness in BSE imaging [see panel (e)]. Panels (g, h) show filamentous sheaths passing across grain boundaries (indicated by arrows). (i, j) Frayed organic filaments within pyrite. Upper arrows indicate a strand emerging from pyrite. Lower arrows delineate a larger filamentous structure, with the left arrow indicating its frayed tip. (k) Raman spectra of the microstructures in panels (a, e). The band at c. 1085 cm^{-1} relates to siderite-rhodochrosite carbonate (Kim et al., 2021). Brt, barite; Py, pyrite; Qtz, quartz.

5.2 | Biogenicity of the pyritic Dresser stromatolites

How do the examined Dresser materials align with the biogenicity concepts in Section 5.1? These pyritic structures, which occur in strata reflecting habitable environments (see also Sections 5.4 and 5.5), escaped penetrative strain, effectively ruling out their formation by deformational processes. The morphologies, textures, and relationships with the host strata in sample S1, featuring chromite-bearing volcanic sandstone draped over and filling the spaces between columnar to domal stromatolites, support this conclusion. These pyritic structures lie atop stratiform pyrite, which lacks signs of significant post-depositional modification, including soft-sediment deformation (see Figures 1b,c, 2a, 7c,d). Additionally, the columnar-domal stromatolites display convex-upward, wavy to wrinkly laminations with crestal thickening (Figure 7), characteristics suggesting stromatolite accretion in shallow water environments. Thus, the morphologies and textural complexities of these stromatolites resemble those described in surface outcrops (e.g., Buick et al., 1981; Hickman-Lewis et al., 2023; Van Kranendonk, 2011; Walter et al., 1980).

Sample S2 provides the strongest evidence of interplays between microbial activity and depositional processes. Here, millimeter-scale columnar pyritic stromatolites, spaced c. 1 cm apart, occupy finely laminated stratum that shows clear evidence of sediment accumulation during stromatolite growth. Specifically, these structures, which rise to c. 5 mm above stratiform pyrite, dictate the cross-stratified bedding in the intercolumn spaces, in stark contrast to the overlying, planar bedded stratum (Figure 4a–c). Microscopic observations support these interpretations, revealing poorly sorted sediment transitioning into finer laminated sediment at the tops of the columns (1 in Figure 4d). Additionally, wrinkly pyritic laminates onlap at the crests (2 in Figure 4d). These textures, which are distinct from ordinary physical sedimentary structures like ripple marks, imply that stromatolite accretion occurred in a dynamic shallow-water setting influenced by water currents (Figure 4c). Thus, they illustrate the interplay between microbial activity and physical depositional processes [supporting evidence (i) and (ii); see Section 5.1]. In this example, vertical growth influenced sedimentation, with initial accumulation of poorly sorted sediment on the high-energy sides of the growing columns and deposition of cross-stratified, thinner laminated sediment at the low-energy sides. Vertical growth may have been prompted by changes in sedimentation rate, water depth, current condition, mineral precipitation rate, nutrient availability, incident sunlight, or combinations of these factors (e.g., Dupraz et al., 2006; Grotzinger & Knoll, 1999; Planavsky & Grey, 2008; Riding, 2011).

The observations above strongly suggest that microbial activity formed the columnar and domal pyritic structures in samples S1 and S2. However, when considering only morphology, texture, and relationships with the host strata, microbial origins are less evident for the stratiform, undulatory to columnar-layered or cumulative pyritic structures in samples S3–S5, which occur in hydrothermally influenced units rich in barite (Figures 1e and 5, Figures S4 and S5). Although broad columnar shapes with convex-upwards lamination (Figure 5a,c) occur, distinguishing them from non-biological mimics remains challenging. Abiotic counterparts include inorganic precipitated mineral crusts (Riding, 2011) and reniform/colloform-banded sulfide precipitates in marine hydrothermal systems (e.g., Maslennikov et al., 2017). This uncertainty is compounded by the growth of barite crystals. The associated deformation, shearing, and truncation of pyritic laminae contributed to the formation of irregular dome-like structures on barite crystal tips (Figure 5d,e). These structures differ from bona fide columnar and domal stromatolites, whose original morphology remained unaffected (Figures 1c, 2a, 7c,d).

Nevertheless, the mostly stratiform structures in samples S3–S5 exhibit significant evidence of microbial influence, particularly through their mineralogical composition and the presence of abundant OM in their interiors. Mirroring the stromatolites in samples S1 and S2, the OM occurs within mineral-organic associations consisting of nanoporous pyrite and microspherulitic barite (Figure 6). The thermal maturity of the OM, estimated at c. 270–280°C (see Figure 7b and Section 4.2), broadly aligns with the main metamorphic overprint of the Dresser Formation, with temperatures around 290°C during a 3.25 Ga metamorphic event (Caruso et al., 2021). The importance of OM-rich nanoporous pyrite was emphasized by Baumgartner et al. (2019). Considering similar OM-rich pyrite microtextures observed in younger rocks (e.g., Wacey et al., 2015), this pyrite generation presumably reflects precipitation onto microbial substrates. Conversely, the microspherulitic morphology of barite (Figure 6j–n; see Baumgartner, Van Kranendonk, Fiorentini, et al., 2020, their figure 3) indicates barite precipitation under low-temperature conditions, facilitated by microbial activity and/or

derived OM, as observed in recent marine systems (e.g., González-Muñoz et al., 2003, 2012; Smith et al., 2004; Stevens et al., 2015).

The above inferences are supported by the C stable isotope data of the OM within the pyritic Dresser stromatolites [$\delta^{13}C_{org} = -29.6‰ \pm 0.3‰$ VPDB (Vienna Peedee belemnite); Baumgartner et al., 2019]. While pyritization is uncommon among Precambrian microbialites, pyrite precipitation has been observed at the base of low-oxygen microbial mats (e.g., Gomes et al., 2022). Additionally, precipitation on biofilms, promoting pyritization of the microbial substrate, occurs in marine hydrothermal systems enriched in H_2S and SO_4^{2-} (e.g., Baumgartner et al., 2022). For the Dresser stromatolites, influence by shallow marine hydrothermal activity is supported by the S stable isotope signature of pyrite, indicating influence by (i) reduced S, probably mainly H_2S, sourced from hydrothermal fluids; and (ii) (microbial) reduction of SO_4^{2-} derived from seawater and hydrothermal activity (see Sections 5.4 and 5.5; Baumgartner, Caruso, Fiorentini, et al., 2020). Therefore, the precipitation of pyrite and barite likely commenced during sedimentation and stromatolite accretion, or shortly thereafter, during early diagenesis and hydrothermal overprinting in the subsurface (see Sections 5.4 and 5.5).

Considering the potential for abiotic hydrocarbon synthesis in hydrothermally influenced settings, additional investigation is necessary to discern the origins of the OM within the Dresser stromatolites. The hydrothermal alteration of mafic to ultramafic rocks in the Dresser Formation's footwall (North Star Basalt; Figure S1) could have released H_2 for the transformation of CO or CO_2 into hydrocarbons, through processes like Fischer-Tropsch synthesis (e.g., Baumgartner et al., 2023; Duda et al., 2018; McCollom et al., 1999; McCollom & Bach, 2009). Although OM is common within the hydrothermal veins beneath the Dresser Formation, two independent studies support a biological origin based on C stable isotope and organic molecular data (Duda et al., 2018; Morag et al., 2016). These findings align with the observations in this study. The OM is scarce in the host strata but occurs in high quantities within the pyritic stromatolites, associated with early formed organomineralization (nanoporous pyrite and microspherulitic barite) that are overgrown by smooth pyrite devoid of OM (Figures 6 and 8 and Figure S8). Additionally, these organics occur independently from potential pathways for post-depositional hydrocarbon migration, such hydrothermal veinlets, fissures, or fractures.

In conclusion, the columnar and domal pyritic Dresser stromatolites meet the morphological criteria for biogenicity. Their characteristics contrast markedly with the host strata, highlighting that abiotic processes alone are insufficient to explain their origin. Fine-scale sediment-stromatolite interference textures provide direct evidence for dynamic interplays between microbial activity and depositional processes. The stromatolites contain significant quantities of demonstrably indigenous OM, consistently present throughout their interiors across various morphologies, from columnar and domal to stratiform structures. Consequently, this elevated OM content serves as a defining feature that, along with distinctive morphology, texture, and mineralogy, distinguishes the stromatolites from the host strata. The OM is trapped within early formed mineral-organic assemblages, predominantly nanoporous pyrite and microspherulitic barite, which dominate the stromatolites. Remarkably, some of the remnant OM resembles the EPS of microorganisms (see Section 5.3).

5.3 | Interpretation of organic microfilaments

Most of the OM occurs as irregular aggregates within nanoporous pyrite (Figure 6d–i). Additionally, the stromatolites host organic filamentous microstructures (Figure 10). Consistent with the filaments reported by Baumgartner et al. (2019, their figure 4), those in this study always occur within nanoporous pyrite, transitioning into or lying next to irregular OM particles with identical Raman spectral signatures (compare the spectra in Figure 10k with those in Figure 7a,b and Figure S6a). These observations, along with the high thermal maturity of the OM (c. 270–280°C, estimated; see Section 4.2), and the partially pyritic composition of some filaments after nitric acid etching (Figure 10e,g), indicate their indigenous nature, entombed within pyrite.

Notably, the observed organic microstructures resemble the degraded EPS of microbes (e.g., Broughton, 2023; Liu et al., 2017; Sprachta et al., 2001). Similar to comparably sized EPS sheaths formed by filamentous microbes (e.g., Bayley et al., 2013, their figure 1b; Liu et al., 2017, their figure 9b), the tubular filamentous sheath in Figure 10a–d is partially collapsed (Figure 10a; indicated as 1 in Figure S9a) and axially torn (see Figure 10b and 2 in Figure S9a,b), with irregular bundles of nanoscopic strands (see Figure 10b and 3 in Figure S9a,b). Other instances include smooth filamentous sheaths grading into irregular bundled filaments (Figure 10g–j; 4 and 5 in Figure S9). Comparable microstructures, representing partially degraded EPS, have been reported from microbialites formed by filamentous phototrophic microorganisms (e.g., Sprachta et al., 2001; Broughton, 2023; Figure S9c). In these examples, polysaccharides are voluminous, providing physical and chemical stability, and contributing to the preservation of the microbial mats during lithification (Decho & Gutierrez, 2017; Sprachta et al., 2001).

The features documented in this study, and ancient organic microstructures elsewhere interpreted as fossilized EPS (e.g., Westall et al., 2006, their figures 4 and 7; Westall et al., 2011, their figure 2), require effective taphonomic processes, such as calcification (e.g., Westall et al., 2011) and pyritization (e.g., Baumgartner et al., 2019; Schieber, 2002). Our results align with preservation through pyritization, as evidenced by the occurrence of the organic microfilaments encased within early precipitated pyrite (Figure 10). However, the identification of these microstructures as remnant EPS remains uncertain, given their scarcity and irregularity. Additionally, similar organic features have been generated abiotically in experiments under sulfidic conditions (e.g., Cosmidis & Templeton, 2016).

Nevertheless, the observed microstructures display striking similarities to the organic microfilaments in the pyritic Dresser stromatolites reported by Baumgartner et al. (2019), both in terms of their micromorphology and viscoelastic property. These characteristics,

which are evidenced by the complex flexing and bundling of microstrands (see Figure 10 and Baumgartner et al., 2019, their figure 4), are typical for malleable EPS (e.g., Klapper et al., 2002), but have not been documented in abiotic organic filaments. These abiotic examples typically exhibit a greater rigidity, with a reduced tangling over several microns rather than the sub-micron scale (Cosmidis & Templeton, 2016, their figures 2–6, and Nims et al., 2021, their figures 1 and 2). These observations suggest that the filamentous structures within the Dresser stromatolites represent remnants of microbial EPS, but conclusive evidence demands further investigation.

5.4 | Environment of stromatolite growth

The examined Dresser stromatolites are notable for their pyritic composition and occurrence within hydrothermally influenced strata, characteristics that are uncommon among microbialites of any age. Notably, these pyritic microbialites contrast with the stromatolites in meta-dolomites from the c. 3.43 Ga Strelley Pool Formation (Allwood et al., 2006, 2009; Hofmann et al., 1999), which formed in shallow marine environments without direct hydrothermal input (Allwood et al., 2006; Van Kranendonk, 2011). Initial studies proposed the Dresser stromatolites formed in a similar paleoenvironment – a quiet, semi-restricted, shallow marine lagoon characterized by intense evaporative cycles (Buick et al., 1981; Buick & Dunlop, 1990; Groves et al., 1981; Walter et al., 1980). However, in this model, the hydrothermal chert-barite veins underlying the Dresser Formation were misinterpreted as post-depositional, emplaced into much younger structures. More recent research, including observations in this study (see Figure 1 and Figure S2, the drill core descriptions in Section 4.1 and Appendix S1), documents rapid facies variations and evidence of hydrothermally influenced sedimentary deposition, suggesting formation in a dynamic, tectonically active environment. This setting also led to subaerial hot spring deposits, all within an interpreted low-eruptive piecemeal-type volcanic caldera with voluminous hydrothermal fluid flow. This dynamic environment, shaped by magmatic inflation and faulting, resulted in transient shallow marine, highly evaporative, and even terrestrial settings (Figure 11; Caruso et al., 2021; Djokic et al., 2017, 2021, 2024; Harris et al., 2009; Nijman et al., 1998; Tadbiri & Van Kranendonk, 2020; Van Kranendonk, 2006, 2011; Van Kranendonk et al., 2008, 2019; Van Kranendonk & Pirajno, 2004).

Evidence for shallow-water to subaerial deposition of the North Pole Chert member includes: (i) rippled, cross bedded, or graded sandstones, some with desiccation cracks; (ii) coarse volcaniclastic conglomerates, including those formed in fluvial channel deposits; (iii) "zebra rock", an evaporative unit with repeated ankerite-chert couplets and aragonite crystals splays; and (iv) a range of terrestrial hot spring facies (Djokic et al., 2017, 2021, 2024; Otálora et al., 2018;

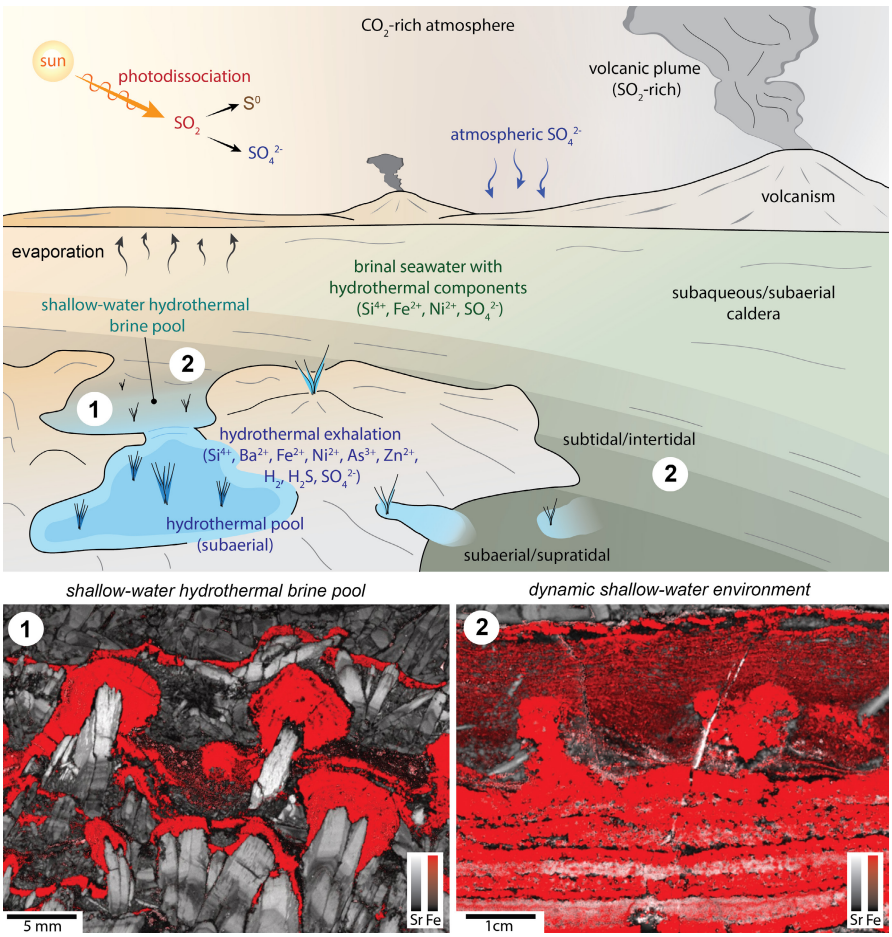

FIGURE 11 Microbial life in a volcanic-sedimentary context with hydrothermal influence. The Dresser stromatolites are interpreted to have formed in shallow marine settings of a volcanic caldera, characterized by strong hydrothermal exhalation and evaporation (see Sections 5.4 and 5.5). The interpreted contexts of microbial growth are: (i) restricted shallow-water hydrothermal brine pools, evidenced by mostly stratiform pyritic structures within barite-rich strata (1); and (ii) dynamic shallow-water environments (2), as indicated by columnar stromatolites that interfere with sedimentary strata. The illustration is based on "The Archean World" by Peter Sawyer, displayed at the Smithsonian Institution. The inset maps (samples S2 and S3) show pyritic microbialites (Fe) and barite crystals (Sr).

Van Kranendonk et al., 2003; Van Kranendonk et al., 2008, 2019, 2021). The zebra rock's formation from evaporating seawater brine is supported by its seawater-like rare earth element (REE)+Y signatures, with concentrations one order of magnitude higher than in similar-aged open marine carbonates. Additionally, elevated Zn and Ba concentrations suggest the presence of intermixed hydrothermal components in the brines, as supported by the strongly negative $\delta^{13}C_{carb}$ signature of the ankerite (Van Kranendonk et al., 2003, 2019, 2021). The hydrothermal discharge occurred predominantly under shallow-water conditions, through upwelling and venting of hydrothermal fluids (Harris et al., 2009; Nijman et al., 1998). It resulted in sedimentary-exhalative units enriched in chert, barite, sulfide and carbonate (Djokic et al., 2017, 2021; Van Kranendonk et al., 2003, 2019; Van Kranendonk & Pirajno, 2004).

Extensive studies have documented the magmatic-hydrothermal processes that influenced the deposition of the Dresser Formation. Investigations of basalts within, beneath, and atop the Dresser Formation, such as the North Star Basalt and Mount Ada Basalt (Figure S1), observed recurring alteration patterns that were interpreted as downward-increasing temperature profiles within stratigraphic packages, progressing from prehnite-pumpellyite to greenschist, and ultimately to amphibolite facies conditions (Terabayashi et al., 2003). These characteristics were attributed to thrust-repeated oceanic slices affected by ocean ridge metamorphism. However, subsequent studies revealed the transformation of basalts below and within the Dresser Formation into argillic assemblages (Van Kranendonk & Pirajno, 2004). This acidic alteration extends to deeper footwall levels at the margins of the hydrothermal veins, transitioning into phyllic, propylitic, and actinolitic assemblages (Caruso et al., 2021). These alteration patterns, in all instances linked to the silica-barite veins, indicate decreasing fluid–rock interactions with increasing distance from the hydrothermal veins (Caruso et al., 2021, 2023). Such characteristics suggest hydrothermal activity driven by a shallow magma chamber. The acidic conditions during argillic alteration require significant contributions of magmatic volatiles (e.g., HCl, SO_2, H_2S, F). Fluid circulation and alteration also leached elements (e.g., Fe, Mg, Ca, Ni, and Zn) from the basalts, which were transported alongside magmatically sourced elements (e.g., S, Ba, and K) within the hydrothermal system. As discussed in Section 5.5, the magmatic-hydrothermal source of Ba was likely crucial for the precipitation of barite within the Dresser Formation (Caruso et al., 2021, 2023).

5.5 | Controls on microbial activity and stromatolite characteristics

The high-quality preservation of the pyritic Dresser stromatolites offers detailed insights into the conditions that supported microbial communities. These microbialites display morphological and textural variabilities alongside facies changes. The columnar to domal stromatolites in sample S1 (Figure 1b,c)thrived under dynamic shallow water conditions (Figure 1l). Consistent with their synoptic relief (Figure 1c), growth ceased through abrupt burial by a chromite-bearing sandstone. This is further supported by the absence of detritral chromite within the stromatolites (Figure 3d), as well as the scarcity of pyrite and OM in the overlying sandstone (Figures 2a and 7). The columnar stromatolites of sample S2 occur within cross-laminated strata, with evidence for growth under shallow water conditions with water currents (Figures 1d and 4). Conversely, the predominantly stratiform forms in samples S3–S5 occur alongside abundant barite, including microcrystalline barite within bedded strata (Figure 5f,g and Figure S5c), and repeated layers of upward-pointing barite crystals that intrude successive pyritic laminae (Figures 1e and 5d–f, Figures S2c and S5). Comparable variations in stromatolite morphology and host lithology have been observed in outcrops: (i) columnar, domal, and conical stromatolites mainly occur in shallow-water deposits with little to no discernible hydrothermal influence; (ii) stratiform structures prevail in strongly hydrothermally influenced units containing horizons of upward-pointing barite crystals and mound-shaped barite deposits (Van Kranendonk, 2006).

The pyritic Dresser stromatolites offer detailed evidence that hydrothermal activity influenced microbial life. Previous studies have documented the genetic relationships between bedded barite mineralization and the hydrothermal veins in the footwall of the Dresser Formation (Baumgartner, van Kranendonk, Pagès, et al., 2020, Djokic et al., 2021, Ueno et al., 2008, Van Kranendonk, 2006, Van Kranendonk et al., 2003, 2008). In the studied samples, upward-pointing barite crystals have deformed, intruded, or engulfed some of the pyritic laminae (Figure 5d–g and Figure S5c). These crystals display marked growth zonations, with upwards increases in Sr concentrations across all crystals within single layers (Figure 5a,b,d,f). Additionally, these crystals are commonly associated with sphalerite (Figure 5a and Figure S5c). Such characteristics align with geochemical modeling results, indicating that large, well-formed, compositionally zoned barite crystals and associated sulfide mineralization (particularly sphalerite) precipitate from moderate to high-temperature (>200°C) hydrothermal fluids (e.g., Jamieson et al., 2016). Consequently, the coarsely crystalline barite observed in this study is interpreted as a hydrothermal-diagenetic precipitate, formed within semi-lithified substrate beneath accreting microbial mats (Baumgartner, van Kranendonk, Pagès, et al., 2020; Van Kranendonk et al., 2008).

Conversely, petrographic and mineralogical evidence, along with observations from modern analogues, suggest the microspherulitic barite (Figure 6j–n) precipitated earlier, perhaps within the brines concurrent with microbial growth. As discussed in Section 5.2, microspherulitic barite, like that in this study, is exclusively known from low-temperature marine settings conducive to microbial life, where microbial activity and OM influence the formation of spherulitic morphologies. Nucleation occurs on cellular surfaces, EPS, or in barite-saturated microenvironments established by OM (see references in Section 5.2). Notably, microspherulitic barite within the stromatolites, similar to the coarsely crystalline barite within the host strata, is less abundant but still significant in samples S1 and S2 compared with samples S3–S5 (see Section 4.2 for details). This

suggests that both barite types formed in the same hydrothermally influenced regimes, albeit with markedly different parageneses, implying asynchronous precipitation. Additionally, the occurrence of microspherulitic barite even within the columnar and domal stromatolites of samples S1 and S2 indicates that their dynamic shallow water environment was significantly influenced, albeit to a lesser extent compared with samples S3–S5, by hydrothermal activity – with hydrothermal fluids having been the primary Ba source for barite precipitation (see Section 5.4).

Figure 12 integrates the above aspects and illustrates the potential relationships between microbial activity and barite precipitation, focussing specifically on sample S3. This specimen exhibits well-developed alternations between bedding-parallel barite layers and OM-rich stromatolitic laminates displaying layer-controlled variations in Ni and As contents (Figure 5a,d,e). The model posits that microbes thrived within concentrated seawater brine pools that were strongly influenced by influxes of hydrothermal fluids (Figure 11). The contained SO_4^{2-} primarily originated from the photodissociation of SO_2 in the O-deficient Archean atmosphere, which was subsequently concentrated in seawater (e.g., Shen et al., 2009; Ueno et al., 2008). Furthermore, the hydrothermally enriched and evaporatively concentrated brines acquired elements like Ca and Sr from both seawater and the hydrothermal alteration of the Dresser Formation's footwall basalts (Figure S1 and Figure 12). Other elements, including Ba and significant Sr, were derived from magmatic fluids that mixed with seawater within the Dresser hydrothermal system (Caruso et al., 2021, 2023).

Considering the factors discussed above, barite precipitated through the mixing between Ba-rich hydrothermal fluids ascending from below and dense, SO_4^{2-}-rich brine descending from above (Figure 12). This process occurred in the shallow subsurface, close to the sediment-brine interface. The hydrothermal fluids maintained temperatures of c. 100–150°C or higher at near-surface levels, as estimated from fluid inclusion studies in hydrothermal silica-barite veins connected to the North Pole Chert member (Harris et al., 2009). This mixing process explains both the conformable microcrystalline barite and the subsequent intrusions of large, upward-tapering, compositionally zoned barite crystals (marked as 1 in Figure 12 and observed in Figure 5f,g). Furthermore, even if barite undersaturation prevailed in the hydrothermally influenced brines, microspherulitic barite might have precipitated locally during stromatolite growth. This is because biomass concentrates Ba^{2+} while OM and microbial activity promote localized barite supersaturation (e.g., Martinez-Ruiz et al., 2018, 2020).

During burial and early diagenesis, decreasing SO_4^{2-} within the brine-filled sediment pore spaces, combined with elevated temperature and the increased solubility of barite due to continuous mixing with hydrothermal fluids, likely created conditions only slightly to moderately saturated with barite. This process would have promoted low nucleation rates but fast crystal growth rates (Deng et al., 2019; Jamieson et al., 2016), facilitating the growth of progressively larger barite crystals that deformed the microbial laminae (indicated as 2 in Figure 12 and observed in Figure 5d,e). Furthermore, hydrothermal influence alongside cycles of brine evaporation in sabkha-style environments would have led to repeated barite crystallization at or just beneath the microbially dominated sediment–water interface. Within each cycle, the enhanced mixing of hydrothermal fluids with the evaporating brines, facilitated by upward percolation or lateral flushing from hydrothermal venting (Figure 12), inhibited microbial growth while facilitating barite precipitation. Thus, as sedimentation progressed, the interplays between cyclical microbial growth, hydrothermal influence, and evaporation collectively contributed to the

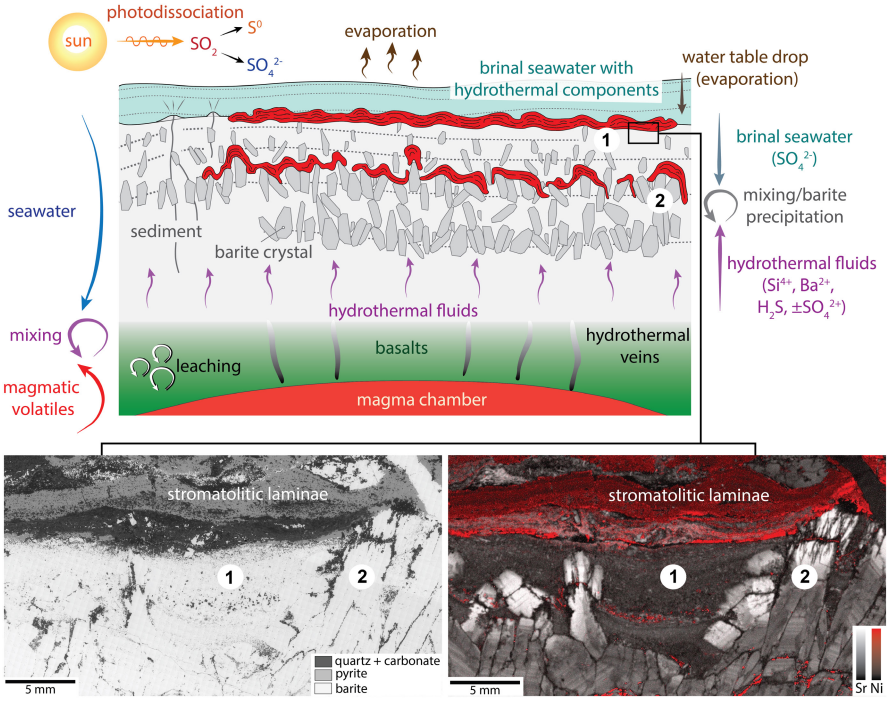

FIGURE 12 Microbial growth in a restricted, hydrothermally influenced shallow water environment (hydrothermal brine pool). The lower panels show a BSE image and an elemental map of pyritic laminae. Indicated are the underlying microcrystalline barite (1) and large barite crystals (2). Figure not drawn to scale.

formation of microbial laminae variably enriched in Ni- and As-rich, interspersed with layers of barite crystals (Figure 5d,e). Additionally, the hydrothermal influx into the unconsolidated sediment sustained barite crystal growth, which led to further deformation of the buried microbial laminae (Figure 12).

Our observations provided concrete evidence that the bedded barite lithofacies of the North Pole Chert member formed through multi-stage barite precipitation driven by complex processes, including hydrothermal activity, interaction with seawater brine, evaporative cycles, and microbial activity. Nevertheless, questions remain regarding the sources of SO_4^{2-}, fluid mixing processes, and the influence of hydrothermal activity on pyrite precipitation. The proposed model (Figure 12) supports the hypothesis that the SO_4^{2-} in Paleoarchean barite deposits originated primarily from Archean seawater (e.g., Muller et al., 2015; Philippot et al., 2012). However, significant amounts likely also came from hydrothermal fluids, as indicated by the S stable isotope signatures of barite and pyrite. The barite crystals display isotopic signatures consistent with their precipitation from a mixture of SO_4^{2-} derived from seawater and the disproportionation of SO_2 within the Dresser hydrothermal system (Ueno et al., 2008). The pyrite in the stromatolites, and that of barite-pyrite assemblages in other sections of the Dresser Formation, exhibit isotopic signatures indicating inputs of hydrothermally sourced H_2S alongside reduced S produced by (microbial) SO_4^{2-} reduction (Baumgartner, Caruso, Fiorentini, et al., 2020; Ueno et al., 2008).

Evidence for hydrothermal contributions of SO_4^{2-} and reduced S also comes from the lithologies underlying the Dresser Formation. As discussed in Section 5.4, the argillic alteration of basalts indicates fluid–rock interactions under acidic conditions, facilitated by magmatically sourced SO_2, which disproportionated into H_2SO_4 and reduced S, particularly S^0 (Caruso et al., 2021, 2023; Van Kranendonk & Pirajno, 2004). However, a limitation in this model is the low solubility of barite in hydrothermal fluids, which likely promoted precipitation at depth and impeded the transportation of SO_4^{2-} and Ba^{2+} to surface levels. Caruso et al. (2021) addressed this issue, proposing that such reactions were inhibited by the binding of Ba^{2+} to metastable silica colloid particles. This mechanism aligns with the Si-rich composition of the hydrothermal veins and the restricted occurrence of barite to c. 75 m below paleosurface levels (Nijman et al., 1998; Ueno, Isozaki, Yurimoto, & Maruyama, 2001; Ueno, Maruyama, Isozaki, & Yurimoto, 2001; Ueno et al., 2008). Thus, Figure 12 represents a comprehensive framework for microbial activity and its relationship to the conditions that promoted barite and pyrite precipitation. Hydrothermal processes transported Ba^{2+} and some SO_4^{2-} to the surface. During microbial growth and later diagenesis, the ongoing mixing of hydrothermal fluids with SO_4^{2-}-rich briny fluids (Figure 12) facilitated the formation of diverse barite types. Pyrite precipitation was driven by (microbial) reduction of SO_4^{2-}, along with H_2S and S^0 derived from hydrothermal fluids.

The model in Figure 12 also helps constrain the origins of the compositionally distinct carbonates associated with the stromatolites. The prevalence of ankerite-dolomite carbonate adjacent to the microbial structures (Figure 8 and Figure S7) suggests a late formation, perhaps during diagenesis and the percolation of hydrothermal fluids within the sediment (Figure 12). Conversely, the minor siderite-rhodochrosite grains within the stromatolites (Figures 6g,l, and 8) imply an earlier formation, possibly under mildly acidic conditions, where some of this carbonate was redissolved amid ongoing hydrothermal influence and pyrite precipitation. A primary origin, through precipitation from concentrated seawater, is particularly relevant for the bedded siderite in sample S4 (Figures S2b and S4a,b), is because the highly ferruginous and anoxic conditions in the Paleoarchean oceans (e.g., Swanner et al., 2020) favored the stability of Fe-rich carbonate.

The $\delta^{13}C_{carb}$ and $\delta^{13}O_{carb}$ data (Figure 9) shed light on these hypotheses. While the isotopic signatures of the siderite-rhodochrosite carbonate within the stromatolites is unknown, the dolomite-ankerite carbonate grains and the bedded siderite in sample S5 exhibit highly negative $\delta^{18}O_{carb}$ values ($\delta^{18}O_{carb}$ c. −10‰ to −13‰ and c. −13‰ to −15‰, respectively). The extremely low $\delta^{18}O_{carb}$ signature of the siderite aligns with precipitation from ^{16}O-depleted Archean seawater (e.g., Lindsay et al., 2005; Shields & Veizer, 2002; Veizer, Hoefs, Lowe, & Thurston, 1989; Veizer, Hoefs, Ridler, et al., 1989). Provided that hydrothermal fluids retained higher $\delta^{18}O$ values from magmatic components (Veizer, Hoefs, Ridler, et al., 1989, and see Section 5.4), the more enriched $\delta^{18}O_{carb}$ value of the dolomite-ankerite carbonate could reflect precipitation from pore fluids comprising brinal seawater and hydrothermal components. Therefore, the ^{13}C depletion in dolomite-ankerite carbonate ($\delta^{13}C_{carb}$ c. −4‰ to −2‰ compared with $\delta^{13}C_{carb}$ c. −0.5‰ for bedded siderite $\delta^{13}C_{carb}$ c. −0.5‰) can be attributed to ^{13}C-depleted inorganic C (e.g., CO_2) sourced by hydrothermal fluids (e.g., Jiang & Tosca, 2022; Kaufman et al., 1990). Alternatively, some ^{13}C-depleted C originated from the thermal decomposition of OM by hydrothermal fluids (e.g., Presley & Kaplan, 1968; Sun et al., 2021), as consistent with the proximity of the dolomite-ankerite carbonate to the OM-rich stromatolites (see Section 4.2 and Figure 8 and Figure S7). However, gaining a better understanding of the factors influencing carbonate precipitation requires further research into carbonates within other units of the Dresser Formation.

5.6 | Hypotheses on microbial functioning and metabolisms

Microbialites form by microbial communities in environments that shape these structures across time and space. Regarding the Dresser stromatolites, an enhanced understanding of the conditions that influenced microbial growth (see Sections 5.4 and 5.5), coupled with the availability of biotic chemistry constituents 3.5 billion years ago (e.g., Van Kranendonk et al., 2021), provide a base for investigating biochemical functioning and metabolic processes.

Primary microbial activity involved anoxygenic photosynthesizers within shallow water environments (see Sections 5.4 and 5.5), which reduced inorganic C (DIC, including CO_2, CO_3^{2-}, HCO_3^-, H_2CO_3) into organic C (Figure 13). This process would have involved

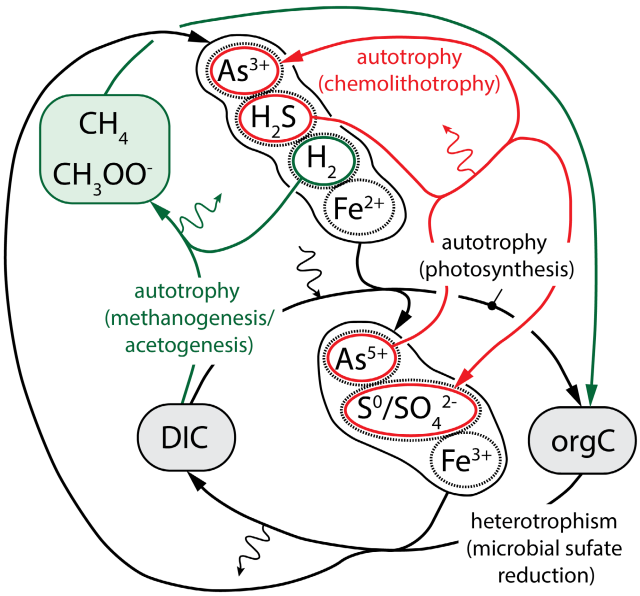

FIGURE 13 Metabolisms cycling C, H, S, As, and Fe compounds. Black indicates: (i) primary productivity by anoxygenic phototrophs, converting inorganic C (DIC: CO_2, CO_3^{2-}, HCO_3^-, and $H_2CO_3^-$) into organic C (orgC); and (ii) respiration of OM by sulfate-reducing microbes. Indicated is the cycling of electron donors (Fe^{2+}, As^{3+}, H_2, and reduced S compounds like H_2S) and electron acceptors (Fe^{3+}, As^{5+}, and S^0/SO_4^{2-}). Green denotes primary productivity by methanogens and acetogens, utilizing H_2 to produce CH_4 and CH_3OO^-. Red indicates chemolithotrophic reduction of As^{5+} coupled with oxidation of reduced S, generating As^{3+} and SO_4^{2-}/S^0. The jagged arrows depict energy inputs/outputs.

the oxidation of Fe^{2+} sourced from anoxic and ferruginous Archean seawater (e.g., Swanner et al., 2020). Other electron donors – including As^{3+} (e.g., Kulp et al., 2008), H_2, and reduced S compounds like $H_2S/HS^-/S_2^-$, polysulfide, elemental S (S^0), and thiosulfate (e.g., Visscher & Van Gemerden, 1993) – potentially originated primarily from hydrothermal activity (see Sections 5.4 and 5.5). Alternatives are methanogenesis and acetogenesis (Figure 13), which entail the oxidation of H_2 (Colman et al., 2022). Evidence is derived from extremely negative $\delta^{13}C$ isotope signatures (as low as −56‰) in C-rich fluid inclusions within the Dresser hydrothermal veins (Ueno et al., 2006), although similarly negative values have not yet been observed within microbialites. Both metabolisms typically rely on Ni for enzymatic processes (e.g., Scheller et al., 2010). The significant Ni within the Dresser pyritic microbialites suggests primary accumulation, along with other metals and metalloids such as As and even Zn, through adsorption onto biomass and/or metabolic processes (Baumgartner, van Kranendonk, Pagès, et al., 2020).

Heterotrophic microorganisms consumed the by-products of primary microbial activity. The significance of microbially formed Fe^{3+} may have been limited due to its low solubility under the assumed pH conditions (≥5) within anoxygenic photosynthetic microbial mats (Pietro-Barajas et al., 2018). However, it is possible that heterotrophic organisms reduced As^{5+}, a by-product of anoxygenic photosynthesis, to As^{3+}, thereby completing As cycling (Sancho-Tomás et al., 2020; Visscher et al., 2020). This mechanism, along with diagenetic processes (cf. Baumgartner, Caruso, Fiorentini, et al., 2020), would have promoted the accumulation of As (Figures 3c and 5d,f and Figure S5c). A similar hypothesis has been proposed for the significant As accumulations in the stromatolites of the c. 2.72 Ga Tumbiana Formation (Sforna et al., 2014). Additionally, chemolithotrophic As^{5+} reduction can be linked to the oxidation of S (Hoeft et al., 2004), providing energy for C fixation while generating SO_4^{2-} and S^0 (Figure 13).

The derived S^0 could have supported microbial S disproportionation (Böttcher et al., 2001), consistent with some S stable isotope fractionation patterns reported from the Dresser Formation and its stromatolites (Baumgartner, Caruso, Fiorentini, et al., 2020; Philippot et al., 2007). Conversely, sulfate-reducing microbes, inferred as having been present through evidence from stromatolites and other sites in the Dresser Formation (e.g., Baumgartner, Caruso, Fiorentini, et al., 2020; Shen et al., 2009; Ueno et al., 2008), drove biomass respiration. These organisms utilized SO_4^{2-} derived from seawater and hydrothermal activity, as well as the SO_4^{2-} generated by anoxygenic photosynthesis and arsenotrophic chemolithotrophy (see the discussion above and Figure 13). Thus, microbial H_2S production, along with reduced S sourced from hydrothermal fluids, provides an explanation for the pyritic composition of the Dresser stromatolites. This process would have facilitated rapid pyrite precipitation, thus preserving putative microbial remnants within the pyrite (see Section 5.3 and Baumgartner et al., 2019).

Beyond metabolisms involving C, S, As, and Fe, microbes may have cycled additional elements. Evidence from Archean rocks indicates the occurrence of anaerobic N_2 fixation, yielding organic NH_4^+ for complex N cycling (Stüeken et al., 2015). Additionally, microbial O_2 production may have emerged early in the Archean era (Crowe et al., 2013). However, the O_2 levels in the atmosphere and oceans remained low until the Great Oxygenation Event c. 2.35 Ga ago (e.g., Catling & Zahnle, 2020). While cyanobacteria might have emerged in the Paleoarchean, this does not necessitates microbial O_2 production because cyanobacteria are also capable of anoxygenic photosynthesis (Hamilton, 2019). Therefore, attributing the Dresser microbialites to O-dependent metabolisms is currently unwarranted.

6 | SYNOPSIS

The origin of the Dresser stromatolites has long been debated. This study reports extensive evidence supporting their biogenicity, including: (i) the characteristic morphologies and textures, including columnar to domal structures and distinctive laminae with thicken over flexure crests; (ii) the clear contrasts between compositionally distinct stromatolites and contemporaneous abiotic sedimentary textures; (iii) the OM-rich inner architectures, with filamentous organic microstructures resembling fossilized EPS trapped within early formed pyrite; and (iv) chemical and isotopic data indicating growth

and mineral precipitation through microbial activity. These findings, along with evidence for habitable environments, strongly support that microbial communities formed the Dresser stromatolites.

This study also explores the relationships between ancient microbial life and its habitats. The varied morphologies of the pyritic Dresser stromatolites, coupled with evidence for their formation under different conditions, highlight dynamic interactions between microbial communities and the environment, similar to findings for the slightly younger Strelley Pool Formation stromatolites (Allwood et al., 2006). Variations in markers of hydrothermal activity, including microspherulitic barite within the microbialites and diagenetic barite crystals in the host strata, suggest a broad range of habitats. These ranged from dynamic shallow water ecosystems with hydrothermal influence to strongly hydrothermally enriched brine pools with ubiquitous SO_4^{2-} sourced from seawater and hydrothermal activity. Our results also imply that the Dresser Formation's dynamic depositional environment facilitated complex microbial communities, where anoxygenic phototrophs and possibly chemotrophs drove primary productivity, while S-metabolizing microbes respired OM. In particular, vigorous microbial S cycling, combined with the supply of reduced S from hydrothermal activity, offers a coherent explanation for the pyritic composition of the Dresser stromatolites.

This study emphasizes the importance of morphology and texture as indicators of biogenicity, especially when the level of preservation enables detailed documentation of the relationships between microbial accretionary structures (e.g., domal and columnar stromatolites with wavy and crinkly laminations) and adjacent sedimentary textures. Our results also shed light on the broader conditions favorable for life during the Paleoarchean era, although they likely highlight only a fraction of the complexities characterizing ancient life. Microbes thrived in a more diverse range of environments, even within the confines of the Dresser Formation. Evidence includes probable Dresser microbialites in hot spring fields (Djokic et al., 2017, 2021), signals of iron-cycling microbial activity in jaspilitic units (Johnson et al., 2022), and putative microbially induced sedimentary structures (MISS) within sabkha facies (Noffke et al., 2013). Continued research on drill cores from the Dresser Formation promises significant advances in understanding Earth's early microbial life.

ACKNOWLEDGMENTS

The analyzed drill cores were collected by Mt Magnet Drilling. We acknowledge the Nyamal peoples as the traditional custodians of the land on which these drill cores were collected. Funding was provided by a Royal Society of New Zealand Marsden Fund grant (17-UOA-037) awarded to Kathleen Campbell, Martin J. Van Kranendonk, and Diego Guido. We acknowledge the facilities, as well as the scientific and technical assistance of the Australian Microscopy & Microanalysis Research Facility Centre for Microscopy, Characterization and Analysis (UWA). We thank the Spectroscopy Facility and the Electron Microscopy Unit (EMU) at Mark Wainwright Analytical Centre (UNSW) for their assistance during our study. We thank Mark Pearce from CSIRO Mineral Resources, who helped with the acquisition of Maia Mapper data. Both Anne Rich (Spectroscopy Facility, Mark Wainwright Analytical Centre, UNSW) and Hua Li (CMCA, UWA) are thanked for their assistance in Raman Spectroscopy analysis. Fabien Dewilde (Pôle Spectrométrie Océan, Technopôle Brest-Iroise) is acknowledged for conducting the stable isotope analyses of carbonate. Michaela J. Dobson was supported by a University of Auckland – Waipapa Taumata Rau (UoA) – Doctoral Scholarship. A portion of this work was conducted at the Jet Propulsion Laboratory, California Institute of Technology under a contract with the National Aeronautics and Space Administration (80NM0018D0004). Roger Buick is thanked for his editorial handling. The constructive comments by three anonymous reviewers contributed to improving the manuscript.

CONFLICT OF INTEREST STATEMENT

The authors declare that they have no known competing financial interests or personal relationships that could have appeared to influence the work reported in this paper.

DATA AVAILABILITY STATEMENT

The authors confirm that the data supporting the findings of this study are available within the article and its supplementary information. Additional information can be obtained from the authors upon reasonable request.

ORCID

Raphael J. Baumgartner https://orcid.org/0009-0007-0641-3702
Bronwyn L. Teece https://orcid.org/0000-0003-0648-5443

REFERENCES

Allwood, A. C., Grotzinger, J. P., Knoll, A. H., Burch, I. W., Anderson, M. S., Coleman, M. L., & Kanik, I. (2009). Controls on development and diversity of early Archean stromatolites. *Proceedings of the National Academy of Sciences of the United States of America*, *106*, 9548–9555.

Allwood, A. C., Walter, M. R., Kamber, B. S., Marshall, C. P., & Burch, I. W. (2006). Stromatolite reef from the early Archaean era of Australia. *Nature*, *441*, 714–718.

Asanuma, H., Sawaki, Y., Sakata, H., Obayashi, H., Suzuki, K., Kitajima, K., Hirata, T., & Maruyama, S. (2018). U-Pb zircon geochronology of the North Pole Dome adamellite in the eastern Pilbara Craton. *Island Arc*, *27*, e12248.

Awramik, S. M., & Grey, K. (2005). Stromatolites: Biogenicity, biosignatures, and bioconfusion. In R. B. Hoover, G. V. Levin, A. Y. Rozanov, & G. R. Gladstone (Eds.), *Proceedings of the SPIE, astrobiology and planetary missions: SPIE abstracts* (Vol. *5906*, pp. 59060P-1–59060P-2). SPIE.

Böttcher, M. E., Thamdrup, B., & Vennemann, T. W. (2001). Oxygen and sulfur isotope fractionation during anaerobic bacterial disproportionation of elemental sulfur. *Geochimica et Cosmochimica Acta*, *65*, 1601–1609.

Batchelor, M. T., Burne, R. V., Henry, B. I., & Watt, S. D. (2003). Mathematical and image analysis of stromatolite morphogenesis. *Mathematical Geology*, *35*, 789–803.

Baumgartner, R. J., Caruso, S., Fiorentini, M. L., van Kranendonk, M. J., Martin, L., Jeon, H., Pagès, A., & Wacey, D. (2020). Sulfidization

of 3.48 billion-year-old stromatolites of the Dresser Formation, Pilbara Craton: Constraints from in-situ sulfur isotope analysis of pyrite. *Chemical Geology*, *538*, 119488.

Baumgartner, R. J., Hu, S., Van Kranendonk, M. J., & Verrall, M. (2022). Taphonomy of microorganisms and microbial microtextures at sulfidic hydrothermal vents: A case study from the Roman Ruins black smokers, Eastern Manus Basin. *Geobiology*, *20*, 479–497.

Baumgartner, R. J., Teece, B. L., Rasmussen, B., Muhling, J., Rickard, W. D. A., Pejcic, B., Hu, S., Bourdet, J., Caruso, S., Van Kranendonk, M. J., & Grice, K. (2023). Exceptional preservation of OM and iron-organic colloidal mineralization in hydrothermal black smoker-type sulfide mineralization from the Paleoarchean seafloor. *Chemical Geology*, *618*, 121296.

Baumgartner, R. J., Van Kranendonk, M. J., Fiorentini, M. L., Pages, A., Wacey, D., Kong, C., Saunders, M., & Ryan, C. (2020). Formation of micro-spherulitic barite in association with OM within sulfidized stromatolites of the 3.48 billion-year-old Dresser Formation, Pilbara craton. *Geobiology*, *18*, 415–425.

Baumgartner, R. J., van Kranendonk, M. J., Pagès, A., Fiorentini, M. L., Wacey, D., & Ryan, C. (2020). Accumulation of transition metals and metalloids in sulfidized stromatolites of the 3.48 billion-year-old Dresser Formation, Pilbara Craton. *Precambrian Research*, *337*, 105534.

Baumgartner, R. J., Van Kranendonk, M. J., Wacey, D., Fiorentini, M. L., Saunders, M., Caruso, S., Pages, A., Homann, M., & Guagliardo, P. (2019). Nano-porous pyrite and OM in 3.5-billion-year-old stromatolites record primordial life. *Geology*, *47*, 1039–1043.

Bayley, J. V., Corsetti, F. A., Greene, S. E., Crosby, C. H., Liu, P., & Orphan, V. J. (2013). Filamentous sulfur bacteria preserved in modern and ancient phosphatic sediments: Implications for the role of oxygen and bacteria in phosphogenesis. *Geobiology*, *11*, 397–405.

Bosak, T., Moore, K. R., Gong, J., & Grotzinger, J. P. (2021). Searching for biosignatures in sedimentary rocks from early earth and Mars. *Nature Reviews Earth and Environment*, *2*, 490–506.

Brasier, M. D., Green, O. R., Jephcoat, A. P., Kleppe, A. K., Van Kranendonk, M. J., Lindsay, J. F., Steele, A., & Grassineau, N. V. (2002). Questioning the evidence for Earth's oldest fossils. *Nature*, *416*, 76–81.

Broughton, P. L. (2023). Microbial EPS-mediated amorphous calcium carbonate–monohydrocalcite-calcite transformations during early tufa deposition. *Depositional Record*, *9*, 647–674.

Buick, R., & Dunlop, J. S. R. (1990). Evaporitic sediments of early Archaean age from the Warrawoona Group, North Pole, Western Australia. *Sedimentology*, *37*, 247–277.

Buick, R., Dunlop, J. S. R., & Groves, D. I. (1981). Stromatolite recognition in ancient rocks: An appraisal of irregularly laminated structures in an early Archaean chert-barite unit from north pole, Western Australia. *Alcheringa*, *5*, 161–181.

Buick, R., Groves, D., & Dunlop, J. S. R. (1995). A biological origin of described stromatolites older than 3.2 Ga; comment. *Geology*, *23*, 191–192.

Caruso, S., Baumgartner, R. J., Van Kranendonk, M. J., Fiorentini, M. L., & Dosseto, A. (2023). The mobilization of boron and lithium in the hydrothermal system of the ~3.48 Ga Dresser Caldera: A stable isotope perspective. *Chemical Geology*, *616*, 121232.

Caruso, S., Van Kranendonk, M. J., Fiorentini, M. L., & Forster, M. A. (2021). The role of magmatic fluids in the ~3.48 Ga Dresser Caldera, Pilbara Craton: New insights from the geochemical investigation of hydrothermal alteration. *Precambrian Research*, *362*, 106299.

Catling, D. C., & Zahnle, K. J. (2020). The Archean atmosphere. *Science Advances*, *6*, *9*.

Cloud, P., & Morrison, K. (1979). On microbial contaminants, micro-pseudofossils, and the oldest records of life. *Precambrian Research*, *9*, 81–91.

Colman, D. R., Kraus, E. A., Thieringer, P. H., & Boyd, E. S. (2022). Deep-branching acetogens in serpentinized subsurface fluids of Oman. *Proceedings of the National Academy of Sciences of the United States of America*, *119*, e2206845119.

Cosmidis, J., & Templeton, A. S. (2016). Self-assembly of biomorphic carbon/sulfur microstructures in sulfidic environments. *Nature Communications*, *7*, 12812.

Crowe, S. A., Døssing, L. N., Beukes, N. J., Bau, M., Gruger, S. J., Frei, R., & Canfield, D. E. (2013). Atmospheric oxygenation three billion years ago. *Nature*, *501*, 535–538.

Decho, A. W., & Gutierrez, T. (2017). Microbial extracellular polymeric substances (EPSs) in ocean systems. *Frontiers in Microbiology*, *8*, 922.

Deng, N., Stack, A. G., Weber, J., Cao, B., De Yoreo, J. J., & Hu, Y. (2019). Organic–mineral interfacial chemistry drives heterogeneous nucleation of Sr-rich $(Ba_x,Sr_{1-x})SO_4$ from undersaturated solution. *Proceedings of the National Academy of Sciences of the United States of America*, *116*, 13221–13226.

Djokic, T., Van Kranendonk, M. J., Campbell, K. A., Having, J. R., Walter, M. R., & Guido, D. M. (2021). A reconstructed subaerial hot spring field in the ~3.5 billion-year-old Dresser Formation, North Pole Dome, Pilbara Craton, Western Australia. *Astrobiology*, *21*, 1–38.

Djokic, T., van Kranendonk, M. J., Campbell, K. A., Walter, M. R., & Ward, C. R. (2017). Earliest signs of life on land preserved in ca. 3.5 Ga hot spring deposits. *Nature Communications*, *8*, 1–8.

Djokic, T., Bolhar, R., Brengman, L. A., Havig, J., & Van Kranendonk, M. J. (2024). Trace elements (REE + Y) reveal marine, subaerial, and hydrothermal controls on an early Archean habitat for life: The 3.48 Ga volcanic-caldera system of the Dresser Formation, Pilbara Craton. *Chemical Geology*, *644*, 121865.

Duda, J. P., Thiel, V., Bauersachs, T., Mißbach, H., Reinhardt, M., Schäfer, N., Van Kranendonk, M. J., & Reitner, J. (2018). Ideas and perspectives: Hydrothermally driven redistribution and sequestration of early Archaean biomass – The "hydrothermal pump hypothesis". *Biogeosciences*, *15*, 1535–1548.

Duda, J. P., Van Kranendonk, M. J., Thiel, V., Ionescu, D., Strauss, H., Schäfer, N., & Reitner, J. (2016). A rare glimpse of Paleoarchean life: Geobiology of an exceptionally preserved microbial mat facies from the 3.4 Ga Strelley Pool Formation, Western Australia. *PLoS One*, *11*(1), e0147629.

Dupraz, C., Pattisina, R., & Verrecchia, E. R. (2006). Translation of energy into morphology: Simulation of stromatolite morphospace using a stochastic model. *Sedimentary Geology*, *185*, 185–203.

Flannery, D. T., Allwood, A. C., Summons, R. E., Williford, K. H., Abbey, W., Matys, E. D., & Ferralis, N. (2018). Spatially-resolved isotopic study of carbon trapped in ~3.43 Ga Strelley Pool Formation stromatolites. *Geochimica et Cosmochimica Acta*, *223*, 21–35.

Glikson, M., Duck, L. J., Golding, S. D., Hofmann, A., Bolhar, R., Webb, R., Baiano, J. C. F., & Sly, L. I. (2008). Microbial remains in some earliest earth rocks: Comparison with a potential modern analogue. *Precambrian Research*, *164*, 187–200.

Gomes, M. L., Klatt, J. M., Dick, G. J., Grim, S. L., Rico, K. I., Medina, M., Ziebis, W., Kinsman-Costello, L., Sheldon, N. D., & Fike, D. A. (2022). Sedimentary pyrite sulfur isotope compositions preserve signatures of the surface microbial mat environment in sediments underlying low-oxygen cyanobacterial mats. *Geobiology*, *20*, 60–78.

González-Muñoz, M. T., Fernandez-Luque, B., Martinez-Ruiz, F., Ben Chekroun, K., Arias, J. M., Rodriguez-Gallego, M., Martínez-Cañamero, M., De Linares, C., & Paytan, A. (2003). Precipitation of barite by *Myxococcus xanthus*: Possible implications for the biogeochemical cycle of barium. *Applied and Environmental Microbiology*, *69*, 5722–5725.

González-Muñoz, M. T., Martinez-Ruiz, F., Morcillo, F., Martin-Ramos, J. D., & Paytan, A. (2012). Precipitation of barite by marine bacteria: A possible mechanism for marine barite formation. *Geology*, *40*, 675–678.

Grey, K., & Awramik, S. M. (2020). Handbook for the study and description of microbialites: Geological survey of Western Australia. *Bulletin*, *147*, 278.

Grotzinger, J. P., & Knoll, A. H. (1999). Stromatolites in Precambrian carbonates: Evolutionary mileposts or environmental dipsticks? *Annual Review of Earth and Planetary Sciences*, *27*, 313–358.

Grotzinger, J. P., & Rothman, D. H. (1996). An abiotic model for stromatolite morphogenesis. *Nature*, *383*, 423–425.

Groves, D. I., Dunlop, J. S. R., & Buick, R. (1981). An early habitat of life. *Scientific American*, *245*, 64–73.

Hamilton, T. L. (2019). The trouble with oxygen: The ecophysiology of extant phototrophs and implications for the evolution of oxygenic photosynthesis. *Free Radical Biology & Medicine*, *140*, 233–249.

Harris, A. C., White, N. C., McPhie, J., Bull, S. W., Line, M. A., Skrzeczynski, R., Mernagh, T. P., & Tosdal, R. M. (2009). Early Archean hot springs above epithermal veins, north pole, Western Australia: New insights from fluid inclusion microanalysis. *Economic Geology*, *104*, 793–814.

Hickman-Lewis, K., Cavalazzi, B., Giannoukos, K., D'Amico, L., Vrbaski, S., Saccomano, G., Dreossi, D., Tromba, G., Foucher, F., Brownscombe, W., Smith, C. L., & Westall, F. (2023). Advanced two- and three-dimensional insights into Earth's oldest stromatolites (ca. 3.5 Ga): Prospects for the search for life on Mars. *Geology*, *51*, 33–38.

Hoeft, S. E., Kulp, T. R., Stolz, J. F., Hollibaugh, J. T., & Oremland, R. S. (2004). Dissimilatory arsenate reduction with sulfide as electron donor: Experiments with mono lake water and isolation of strain MLMS-1, a chemoautotrophic arsenate respirer. *Applied and Environmental Microbiology*, *70*, 2741–2747.

Hofmann, H. J., Grey, K., Hickman, A. H., & Thorpe, R. I. (1999). Origin of 3.45 Ga coniform stromatolites in Warrawoona group, Western Australia. *Geological Society of America Bulletin*, *111*, 1256–1262.

Jahnert, R. J., & Collins, L. B. (2012). Characteristics, distribution, and morphogenesis of subtidal microbial systems in Shark Bay, Australia. *Marine Geology*, *303–306*, 115–136.

Jamieson, J. W., Hannington, M. D., Tivey, M. K., Hansteen, T., Williamson, N. M. B., Stewart, M., Fietzke, J., Butterfield, D., Frische, M., Allen, L., Cousens, B., & Langer, J. (2016). Precipitation and growth of barite within hydrothermal vent deposits from the Endeavour Segment, Juan de Fuca ridge. *Geochimica et Cosmochimica Acta*, *173*, 64–85.

Jiang, C. Z., & Tosca, N. J. (2022). Fe(II)-carbonate precipitation kinetics and the chemistry of anoxic ferruginous seawater. *Earth and Planetary Science Letters*, *506*, 231–242.

Johnson, C. M., Zheng, X. Y., Djokic, T., Van Kranendonk, M. J., Czaja, A. D., Roden, E. E., & Beard, B. L. (2022). Early Archean biogeochemical iron cycling and nutrient availability: New insights from a 3.5 Ga land-sea transition. *Earth-Science Reviews*, *228*, 103992.

Kalkowsky, E. (1908). Oolith und Stromatolith im norddeutschen Buntsandstein. *Zeitschrift der Deutschen Geologischen Gesellschaft*, *60*, 68–125.

Kaufman, A. J., Hayes, J. M., & Klein, C. (1990). Primary and diagenetic controls of isotopic compositions of iron-formation carbonates. *Geochimica et Cosmochimica Acta*, *54*, 3461–3473.

Kim, Y., Caumon, M. C., Barres, O., Sall, A., & Cauzid, J. (2021). Identification and composition of carbonate minerals of the calcite structure by Raman and infrared spectroscopies using portable devices. *Spectrochimica Acta. Part A, Molecular and Biomolecular Spectroscopy*, *261*, 119980.

Klapper, I., Rupp, C. J., Cargo, R., Purvedorj, B., & Stoodley, P. (2002). Viscoelastic fluid description of bacterial biofilm material properties. *Biotechnology and Bioengineering*, *80*, 289–296.

Kouketsu, Y., Mizukami, T., Mori, H., Endo, S., Aoya, M., Hara, H., Nakamura, D., & Wallis, S. (2014). A new approach to develop the Raman carbonaceous material geothermometer for low-grade metamorphism using peak width. *Island Arc*, *23*, 33–50.

Krumbein, W. E. (1983). Stromatolites: The challenge of a term in space and time. *Precambrian Research*, *20*, 493–531.

Kulp, T. R., Hoeft, S. E., Asao, M., Madigan, M. T., Hollibaugh, J. T., Fisher, J. C., Stolz, J. F., Culbertson, C. W., Miller, L. G., & Oremland, R. S. (2008). Arsenic(III) fuels anoxygenic photosynthesis in hot spring biofilms from mono Lake, California. *Science*, *321*, 967–970.

Lepot, K. (2020). Signatures of early microbial life from the Archean (4 to 2.5 Ga) eon. *Earth-Science Reviews*, *209*, 103296.

Lepot, K., Benzerara, K., Brown, G. E., & Philippot, P. (2008). Microbially influenced formation of 2,724-million-year-old stromatolites. *Nature Geoscience*, *1*, 118–121.

Lindsay, J. F., Brasier, M. D., McLoughlin, N., Green, O. R., Fogel, M., Steele, A., & Mertzman, S. A. (2005). The problem of deep carbon – An Archean paradox. *Precambrian Research*, *143*, 1–22.

Liu, S., Wang, J., Yin, F., Xie, T., Hu, S., Guan, X., Zhang, Q., Zhou, C., Cheng, W., & Xu, J. (2017). Early Triassic stromatolites from the Xingyi area, Guizhou Province, southwest China: Geobiological features and environmental implications. *Carbonates and Evaporites*, *32*, 261–277.

Lowe, D. R. (1980). Stromatolites 3,400-Myr old from the Archean of Western Australia. *Nature*, *284*, 441–443.

Lowe, D. R. (1994). Abiological origin of described stromatolites older than 3.2 Ga. *Geology*, *22*, 387–390.

Marin-Carbonne, J., Remusat, L., Sforna, M. C., Thomazo, C., Cartigny, P., & Phillipot, P. (2018). Sulfur isotope's signal of nanopyrites enclosed in 2.7 Ga stromatolitic organic remains reveal microbial sulfate reduction. *Geobiology*, *16*, 121–138.

Martinez-Ruiz, F., Jroundi, F., Paytan, A., Guerra-Tschuschke, I., Abad, M. M., & González-Muñoz, M. T. (2018). Barium bioaccumulation by bacterial biofilms and implications for Ba cycling and use of Ba proxies. *Nature Communications*, *9*, 1619.

Martinez-Ruiz, F., Paytan, A., González-Muñoz, M. T., Jroundi, F., Abad, M. M., Lam, P. J., Horner, T. J., & Kastner, M. (2020). Barite precipitation on suspended OM in the mesopelagic zone. *Frontiers in Earth Science*, *8*, 567714.

Maslennikov, V. V., Maslennikova, S. P., Large, R. R., Danyushevsky, L. V., Herrington, R. J., Ayupova, N. R., Zaykov, V. V., Lein, A. Y., Tseluyko, A. S., Melekestseva, I. Y., & Tessalina, S. G. (2017). Chimneys in Palaeozoic massive sulfide mounds of the Urals VMS deposits: Mineral and trace element comparison with modern black, grey, white and clear smokers. *Ore Geology Reviews*, *85*, 64–106.

McCollom, T. M., & Bach, W. (2009). Thermodynamic constraints on hydrogen generation during serpentinization of ultramafic rocks. *Geochimica et Cosmochimica Acta*, *73*, 856–875.

McCollom, T. M., Ritter, G., & Simoneit, B. R. T. (1999). Lipid synthesis under hydrothermal conditions by Fischer-Tropsch-type reactions. *Origins of Life and Evolution of the Biosphere*, *29*, 153–166.

McLoughlin, N., Wilson, L. A., & Brasier, M. D. (2008). Growth of synthetic stromatolites and wrinkle structures in the absence of microbes – Implications for the early fossil record. *Geobiology*, *6*, 95–105.

Morag, N., Williford, K. H., Kitajima, K., Philippot, P., Van Kranendonk, M. J., Lepot, K., Thomazo, C., & Valley, J. W. (2016). Microstructure-specific carbon isotopic signatures of OM from ~3.5 Ga cherts of the Pilbara Craton support a biologic origin. *Precambrian Research*, *275*, 429–449.

Muller, É., Philippot, P., Rollion-Bard, C., & Cartigny, P. (2015). Multiple sulfur-isotope signatures in Archean sulfates and their implications for the chemistry and dynamics of the early atmosphere. *Proceedings of the National Academy of Sciences of the United States of America*, *113*, 7432–7437.

Neveu, M., Hays, L. E., Voytek, M. A., New, M. H., & Schulte, M. D. (2018). The ladder of life detection. *Astrobiology*, *18*, 1375–1402.

Nijman, W., De Bruin, K., & Valkering, M. (1998). Growth fault control of early Archaean cherts, barite mounds, and chert–barite veins,

North Pole Dome, Eastern Pilbara, Western Australia. *Precambrian Research*, *88*, 25–52.

Nims, C., Lafond, J., Alleon, J., Templeton, A. S., & Cosmidis, J. (2021). Organic biomorphs may be better preserved than microorganisms in early earth sediments. *Geology*, *49*, 629–634.

Noffke, N., Christian, D., Wacey, D., & Hazen, R. M. (2013). Microbially induced sedimentary structures recording an ancient ecosystem in the ca. 3.48 billion-year-old Dresser Formation, Pilbara, Western Australia. *Astrobiology*, *13*, 1103–1124.

Otálora, F., Mazurier, A., Garcia-Ruiz, J. M., Van Kranendonk, M. J., Kotopoulou, E., El Albani, A., & Garrido, C. J. (2018). A crystallographic study of crystalline casts and pseudomorphs from the 3.5 Ga Dresser Formation, Pilbara Craton (Australia). *Journal of Applied Crystallography*, *51*, 1050–1058.

Philippot, P., Van Zuilen, M., Lepot, K., Thomazo, C., Farquhar, J., & van Kranendonk, M. J. (2007). Early Archaean microorganisms preferred reduced sulfur, not sulfate. *Science*, *317*, 1534–1537.

Philippot, P., Van Zuilen, M., & Rollion-Bard, C. (2012). Variations in atmospheric sulphur chemistry on early earth linked to volcanic activity. *Nature Geoscience*, *5*, 668–674.

Pietro-Barajas, C. M., Valencia-Cantero, E., & Santoyo, G. (2018). Microbial mat ecosystems: Structure types, functional diversity, and biotechnological application. *Electronic Journal of Biotechnology*, *31*, 48–56.

Planavsky, N., & Grey, K. (2008). Stromatolite branching in the Neoproterozoic of the Centralian Superbasin, Australia: An investigation into sedimentary and microbial control of stromatolite morphology. *Geobiology*, *6*, 33–45.

Presley, B. J., & Kaplan, I. R. (1968). Changes in dissolved sulfate, calcium and carbonate from interstitial water of near shore sediments. *Geochimica et Cosmochimica Acta*, *32*, 1037–1049.

Riding, R. (2011). Microbialites, stromatolites, and thrombolites. In J. Reitner & V. Thiel (Eds.), *Encyclopedia of geobiology. Encyclopedia of earth science series* (pp. 635–654). Springer.

Runnegar, B., Dollase, W. A., Ketcham, R. A., Colbert, M., & Carlson, W. D. (2001). Early Archaean sulphates from Western Australia first formed as hydrothermal barite not gypsum evaporates. *Geological Society of America Abstracts*, *33*, A-404.

Sancho-Tomás, M., Somogyi, A., Medjoubi, K., Bergamaschi, A., Visscher, P. T., Van Driessche, A. E. S., Gerard, E., Farias, M. E., Contreras, M., & Philippot, P. (2020). Geochemical evidence for arsenic cycling in living microbialites of a high altitude Andean Lake (Laguna Diamante, Argentina). *Chemical Geology*, *549*, 119681.

Scheller, S., Goenrich, M., Böcher, R., Thauer, R. K., & Jaun, B. (2010). The key nickel enzyme of methanogenesis catalyses the anaerobic oxidation of methane. *Nature*, *465*, 606–608.

Schieber, J. (2002). Sedimentary pyrite: A window into the microbial past. *Geology*, *30*, 531–534.

Schopf, W. J., & Packer, B. M. (1987). Early Archean (3.3-billion to 3.5-billion-year-old) microfossils from Warrawoona Group, Australia. *Science*, *237*, 70–73.

Semikhatov, M. A., Gebelein, C. D., Cloud, P., Awramik, S. M., & Benmore, W. C. (1979). Stromatolite morphogenesis – Progress and problems. *Canadian Journal of Earth Sciences*, *16*, 992–1015.

Sforna, M. C., Philippot, P., Somogyi, A., Van Zuilen, M. A., Medjoubi, K., Schoepp-Cothenet, B., Nitschke, W., & Visscher, P. T. (2014). Evidence for arsenic metabolism and cycling by microorganisms 2.7 billion years ago. *Nature Geoscience*, *7*, 811–815.

Shen, Y., Buick, R., & Canfield, D. E. (2001). Isotopic evidence for microbial sulphate reduction in the early Archaean era. *Nature*, *410*, 77–81.

Shen, Y., Farquhar, J., Masterson, A., Kaufman, A. J., & Buick, R. (2009). Evaluating the role of microbial sulfate reduction in the early Archean using quadruple isotope systematics. *Earth and Planetary Science Letters*, *279*, 383–391.

Shields, G., & Veizer, J. (2002). Precambrian marine carbonate isotope database: Version 1.1. *Geochemistry, Geophysics, Geosystems*, *3*, *6*.

Smith, E., Hamilton-Taylor, J., Davison, W., Fullwood, N. J., & McGrath, M. (2004). The effect of humic substances on barite precipitation–dissolution behaviour in natural and synthetic lake waters. *Chemical Geology*, *207*, 81–89.

Sprachta, S., Camoin, G., Golubic, S., & Le Champion, T. (2001). Microbialites in a modern lagoonal environment: Nature and distribution, Tikehau atoll (French Polynesia). *Palaeogeography Palaeoclimatology Palaeoecology*, *26*, 433–450.

Stüeken, E. E., Buick, R., Guy, B. M., & Koehler, M. C. (2015). Isotopic evidence for biological nitrogen fixation by molybdenum-nitrogenase from 3.2 Gyr. *Nature*, *520*, 666–669.

Stevens, E. W. N., Bailey, J. V., Flood, B. E., Jones, D. S., Gilhooly, W. P., Joye, S. B., Teske, A., & Mason, O. U. (2015). Barite encrustation of benthic sulfur-oxidizing bacteria at a marine cold seep. *Geobiology*, *13*, 588–603.

Sun, F., Hu, W., Wu, H., Fu, B., Wang, X., Tang, Y., Cao, J., Yang, S., & Hu, Z. (2021). Two-stage mineral dissolution and precipitation related to organic matter degradation: Insights from in situ C–O isotopes of zoned carbonate cements. *Marine and Petroleum Geology*, *124*, 104812.

Swanner, E. D., Lambrecht, N., Wittkop, C., Harding, C., Katsev, S., Torgeson, J., & Poulton, S. W. (2020). The biogeochemistry of ferruginous lakes and past ferruginous oceans. *Earth-Science Reviews*, *211*, 103430.

Tadbiri, S., & Van Kranendonk, M. J. (2020). Structural analysis of syn-depositional hydrothermal veins of the 3.48 Ga Dresser Formation, Pilbara Craton, Australia. *Precambrian Research*, *347*, 105844.

Terabayashi, M., Masuda, Y., & Ozawa, H. (2003). Archean ocean-floor metamorphism in the North Pole area, Pilbara Craton, Western Australia. *Precambrian Research*, *127*, 167–180.

Ueno, Y., Isozaki, Y., Yurimoto, H., & Maruyama, S. (2001). Carbon isotopic signatures of individual Archean microfossils (?) from Western Australia. *International Geology Review*, *43*, 196–212.

Ueno, Y., Maruyama, S., Isozaki, Y., & Yurimoto, H. (2001). Early Archean (ca. 3.5 Ga) microfossils and ^{13}C-depleted carbonaceous matter in the North Pole area, Western Australia: Field occurrence and geochemistry. In S. Nakashima, S. Maruyama, A. Brack, & B. F. Windley (Eds.), *Geochemistry and the origin of life* (pp. 203–236). Universal Academy Press.

Ueno, Y., Ono, S., Rumble, D., & Maruyama, S. (2008). Quadruple sulfur isotope analysis of ca. 3.5 Ga Dresser Formation: New evidence for microbial sulfate reduction in the early Archean. *Geochimica et Cosmochimica Acta*, *72*, 5675–5691.

Ueno, Y., Yamada, K., Yoshida, N., Maruyama, S., & Isozaki, Y. (2006). Evidence from fluid inclusions for microbial methanogenesis in the early Archaean era. *Nature*, *440*, 516–519.

Ueno, Y., Yoshioka, H., Maruyama, S., & Isozaki, Y. (2004). Carbon isotopes and petrography of kerogens in ~3.5-Ga hydrothermal silica dikes in the North Pole area, Western Australia. *Geochimica et Cosmochimica Acta*, *68*, 573–589.

Van Kranendonk, M. J. (2006). Volcanic degassing, hydrothermal circulation and the flourishing of early life on Earth: A review of the evidence from c. 3490-3240 ma rocks of the Pilbara Supergroup, Pilbara Craton, Western Australia. *Earth-Science Reviews*, *74*, 197–240.

Van Kranendonk, M. J. (2011). Stromatolite morphology as an indicator of biogenicity for earth's oldest fossils from the 3.5–3.4 Ga Pilbara Craton, Western Australia. In J. Reitner, N. V. Queric, & G. Arp (Eds.), *Advances in stromatolite geobiology. Lecture notes in earth sciences* (Vol. *131*, pp. 537–554). Springer.

Van Kranendonk, M. J., Djokic, T., Poole, G., Tadbiri, S., Steller, L., & Baumgartner, R. J. (2019). Depositional setting of the fossiliferous, c. 3480 ma Dresser Formation, Pilbara Craton: A review. In M. J.

Van Kranendonk, V. Bennett, & E. Hoffmann (Eds.), *Earth's oldest rocks* (pp. 985–1006). Elsevier.

Van Kranendonk, M. J., Philippot, P., Lepot, K., Bodorkos, S., & Pirajno, F. (2008). Geological setting of Earth's oldest fossils in the ca. 3.5 Ga Dresser Formation, Pilbara Craton, Western Australia. *Precambrian Research*, *167*, 93–124.

Van Kranendonk, M. J., & Pirajno, F. (2004). Geological setting and geochemistry of metabasalts and alteration zones associated with hydrothermal chert ± barite deposits in the ca. 3.45 Ga Warrawoona group, Pilbara Craton, Australia. *Geochemistry: Exploration, Environment, Analysis*, *4*, 253–278.

Van Kranendonk, M. J., Smithies, R. H., Hickman, A. H., & Champion, D. C. (2007). Secular tectonic evolution of Archaean continental crust: Interplay between horizontal and vertical processes in the formation of the Pilbara Craton, Australia. *Terra Nova*, *19*, 1–38.

Van Kranendonk, M. J., Webb, G. E., & Kamber, B. S. (2003). Geological and trace element evidence for a marine sedimentary environment of deposition and biogenicity of 3.45 Ga stromatolitic carbonates in the Pilbara Craton, and support for a reducing Archean ocean. *Geobiology*, *1*, 91–108.

Van Kranendonk, M. J., Baumgartner, R., Djokic, T., Ota, T., Steller, L., Garbe, U., & Nakamura, E. (2021). Elements for the origin of life on land: A deep-time perspective from the Pilbara Craton of Western Australia. *Astrobiology*, *21*, 39–59.

Veizer, J., Hoefs, J., Lowe, D. R., & Thurston, P. C. (1989). Geochemistry of Precambrian carbonates: II. Archean greenstone belts and Archean seawater. *Geochimica et Cosmochimica Acta*, *53*, 859–871.

Veizer, J., Hoefs, J., Ridler, R. H., Jensen, L. S., & Lowe, D. R. (1989). Geochemistry of Precambrian carbonates: I. Archean hydrothermal systems. *Geochimica et Cosmochimica Acta*, *53*, 845–857.

Visscher, P. T., Gallagher, K. L., Bouton, A., Farias, M. E., Kurth, D., Sancho-Tomás, M., Philippot, P., Somogyi, A., Medjoubi, K., Vennin, E., Bourillot, R., Walter, M. R., Burns, B. P., Contreras, M., & Dupraz, C. (2020). Modern arsenotrophic microbial mats provide an analogue for life in the anoxic Archean. *Nature Communications Earth & Environment*, *1*, 24.

Visscher, P. T., & Van Gemerden, H. (1993). Sulfur cycling in laminated marine ecosystem. In R. S. Oremland (Ed.), *Biogeochemistry of global change: Radiatively active trace gases*. Chapman and Hall.

Wacey, D., Kilburn, M. R., Saunders, M., Cliff, J. B., Kong, C., Liu, A. G., Matthews, J. J., & Brasier, M. D. (2015). Uncovering framboidal pyrite biogenicity using nano-scale CN_{org} mapping. *Geology*, *43*, 27–30.

Walter, M. R. (1976). Introduction. In M. R. Walter (Ed.), *Stromatolites* (pp. 1–3). Elsevier.

Walter, M. R., Buick, R., & Dunlop, J. S. R. (1980). Stromatolites 3,400–3,500 Myr old from the North pole area, Western Australia. *Nature*, *284*, 443–445.

Walter, M. R., Grotzinger, J. P., & Schopf, J. W. (1992). Proterozoic stromatolites. In J. W. Schopf & C. Klein (Eds.), *The Proterozoic biosphere: A multidisciplinary study* (pp. 253–260). Cambridge University Press.

Westall, F., Cavalazzi, B., Lemelle, L., Marrocchi, Y., Rouzaud, J. N., Simionovici, A., Salomé, M., Mostefaoui, S., Andreazza, C., Foucher, F., Toporski, J., Jauss, A., Thiel, V., Southam, G., MacLean, L., Wirick, S., Hofmann, A., Meibom, A., Robert, F., & Défarge, C. (2011). Implications of in situ calcification for photosynthesis in a ~3.3 Ga-old microbial biofilm from the Barberton greenstone belt, South Africa. *Earth and Planetary Science Letters*, *310*, 468–479.

Westall, F., De Vries, S. T., Nijman, W., Rouchon, V., Orberger, B., Pearson, V., Watson, J., Verchovsky, A., Wright, I., Rouzaud, J. N., Marchesini, D., & Severine, A. (2006). The 3.466 Ga "kitty's gap chert", an early Archean microbial ecosystem. In W. U. Reimod & R. L. Gibson (Eds.), *Processes on the early earth* (Vol. *405*, pp. 105–131). Geological Society of America Special Papers.

SUPPORTING INFORMATION

Additional supporting information can be found online in the Supporting Information section at the end of this article.

How to cite this article: Baumgartner, R. J., Van Kranendonk, M. J., Caruso, S., Campbell, K. A., Dobson, M. J., Teece, B. L., Verrall, M., Homann, M., Lalonde, S., & Visscher, P. T. (2024). Pyritic stromatolites from the Paleoarchean Dresser Formation, Pilbara Craton: Resolving biogenicity and hydrothermally influenced ecosystem dynamics. *Geobiology*, *22*, e12610. https://doi.org/10.1111/gbi.12610